Evaluation of Cavitation Abrasive Surface Finishing as a Surface Treatment for Metal Produced Through Laser Powder Bed Fusion

Rohin Petram

A thesis
submitted in partial fulfillment of the
requirements for the degree of
Master of Science

University of Washington
2025

Committee:
Dwayne Arola
Ramulu Mamidala
Daniel Sanders

Program Authorized to Offer Degree:
Material Science and Engineering

University of Washington

Abstract

Evaluation of Cavitation Abrasive Surface Finishing as an Industry Ready Surface Treatment for Metal Produced Through Laser Powder Bed Fusion

Rohin Petram

Chair of the Supervisory Committee:
Dwayne Arola
Department of Materials Science and Engineering

Ramulu Mamidala

Department of Mechanical Engineering

Abstract - Laser powder bed fusion (L-PBF) has emerged as a highly viable method for manufacturing metal structural components across various industries. However, the inherently rough surfaces and complex morphologies of L-PBF components, particularly those with vertical, upskin, and downskin orientations, necessitate post processing treatments to improve surface finish and integrity. Additionally, heat treatments used to control microstructure and mechanical properties often produce a surface oxide layer that requires removal. In this investigation, cavitation abrasive surface finishing (CASF) was employed to improve the surface quality and

remove the oxide layer of LPBF Ti6Al4V components, with specific attention to how build orientation, presence of alpha case, and line of sight effected the ability of CASF to improve the surface texture, introduce residual stress, and remove material. Results showed that CASF reduced the average surface roughness from approximately 5 to 20 μm in the as-built condition (depending on orientation) to as low as 4 μm. The process also imparted compressive residual stresses up to 600 MPa and was capable of removing the alpha case from direct line-of-sight surfaces.

Despite these improvements, treatment uniformity varied with surface orientation. downskin surfaces, characterized by higher initial roughness and more extensive coverage of partially fused powder particles were the most challenging to treat. Even after CASF, these surfaces achieved significantly lower compressive residual stress, apparently due to shielding effects of particles that limit cavitation impact. Overall, CASF demonstrated strong potential as a non-chemical alternative for post processing LPBF titanium components, offering both surface smoothing and beneficial compressive stress. However, optimization of treatment parameters is needed to improve uniformity across orientations and to further assess the fatigue performance of treated surfaces.

Chapter 1. Introduction

Additive manufacturing (AM) is defined by ASTM International as "The process of joining materials to make parts from 3D model data, usually layer upon layer, as opposed to subtractive manufacturing and formative manufacturing methodologies." [1]. Of the many types of additive manufacturing, metal AM has undergone the most rapid growth due to interest in its application to develop structural components. Laser powder bed fusion (LPBF), a specific approach to metal AM, utilizes a high-powered laser to selectively melt metal powder in a layer-by-layer method [2]. By limiting the metal powder consumed relative to that used in the final part volume, LPBF is highly efficient. Consequently, it is well suited for alloys that are expensive and challenging to machine including Inconel, stainless steel, and Ti6Al4V. The printing process results in components that are very near neat shape, thereby eliminating most post-process machining [2-3].

The LPBF process is quickly becoming an important process for the future of the aerospace, biomedical, and automotive industry, but current complications posed by the printed surface quality have restricted the rate of adoption from expanding further. These limitations include high surface roughness, potential oxidization of the surface, and tensile residual stresses on the surface [4-8]. Exacerbating these issues, one key advantage of AM is the near limitless complexity that can be achieved by these machines. As a consequence, parts produced using AM often include surfaces which are not readily accessible by direct line of sight treatments. For LPBF to be more widely adopted, a method of surface treatment must be identified that is capable of treating surfaces regardless of their orientation and with minimal restriction from the geometric complexity [8].

Despite the attractive qualities of AM, many potential applications will not be realized because of i) the prohibitively rough surfaces, and ii) the absence of a way to treat the surface of

AM metal parts [4,10]. A process that can simultaneously reduce surface roughness and introduce compressive residual stress without requiring a direct line of sight of the part will unlock opportunities for AM to be utilized in new applications previously unavailable [4, 10-11]. The most prominent surface treatments used for engineering components include various peening methods and chemical milling. While each treatment has its advantages and disadvantages, currently there is no treatment capable of both smoothing and introducing compressive residual stress simultaneously [12-13]. In addition, the processes capable of introducing compressive residual stress (e.g. shot peening) require line of sight treatment.

1.1 Cavitation Abrasive Surface Finishing

Cavitation Abrasive Surface Finishing (CASF) is a surface treatment method developed to improve the surface texture and surface integrity of metal components produced by any manufacturing process. Due to the critical need, it is now being considered for components produced by metal AM [14]. The CASF process utilizes a high-pressure water jet, submerged in a tank with dilute abrasive slurry. The nozzle and interaction with fluid tank generates a network of cavitating bubbles in an area around its orifice. When these bubbles collapse, they impart kinetic energy into the abrasives and onto the component surface. Movement of the abrasive particles invokes surface smoothing through material removal. Collapse of the cavitation bubbles on the target imparts a compressive residual stress similar to other peening methods [10-14]. CASF has the potential to overcome the limitations of conventional surface treatments, including chemical etching and various peening methods, which will be pursued in the following research.

1.2 Objectives

The research described in this thesis is focused on exploring the application of CASF to titanium components produced by LPBF to decrease surface roughness, remove alpha case, and impart compressive residual stress. The specific objectives are to:

1. Treat the surface of components produced by LPBF that represent specific challenge conditions of importance including upskin, downskin, and vertically printed surfaces.
2. Evaluate the propensity for CASF to reduce the surface roughness and remove surface defects of the printed components with respect to the printed surface orientation
3. Evaluate the ability for CASF to impart compressive residual stress on the surface of treated parts.
4. Evaluate whether CASF can remove the brittle alpha case from the surface of additive manufactured parts that have undergone heat treatment and caused surface oxidation.

Chapter 2. Literature Review

The high strength to weight ratio, resistance to corrosion, and biocompatibility of titanium alloys make them appropriate for many applications, especially in the aerospace and medical device industries [4]. However, the comparatively low ductility, low thermal conductivity, and affinity for oxidation pose significant challenges to the manufacture of complex parts from titanium alloys by traditional methods [15]. This raises the value of AM as a potential manufacturing technique to be used to produce parts made of titanium. Because AM can produce parts in their "very near net-shape" form, they can be produced with limited machining required.

2.1 Laser Powder Bed Fusion

Laser Powder Bed Fusion (LPBF) systems operate by spreading thin layers of metal powder over a build plate. A high-powered laser is used to selectively melt specific regions of each powder layer to form the desired geometry. After each layer is processed, the build plate is lowered, and a new layer of powder is applied on top. This layer-by-layer approach continues until the entire component is completed. LPBF typically involves rapid cooling rates due to localized melting and solidification, which can lead to the formation of a brittle martensitic microstructure in some alloys [16, 17]. This microstructure may contribute to increased residual stress and potential warping during or after the build process. The entire build space must be kept in an inert environment to keep the metal from oxidizing during the solid-liquid-solid transition. As such, argon gas is continuously fed into the sealed build chamber. The argon gas also serves to direct condensate and spatter particles emanating from the melt pool away from beam path and towards the exhaust ducting [18].

While LPBF of titanium alloys offers many advantages, it often results in metal quality that possesses inferior mechanical properties in comparison to wrought titanium, particularly in terms of fatigue resistance [8,9,19,20]. This limitation is largely due to the presence of defects such as gas porosity, lack of fusion, and keyhole-induced voids, which are frequently observed in LPBF builds [20,21]. Additionally, the layer-by-layer melting process results in directional grain structures that cause anisotropic mechanical behavior, with properties varying based on the component orientation relative to the build direction [20, 22-24]. As a result, post-processing heat treatment is generally considered essential to improve material uniformity and mechanical performance [25 - 27].

Hot Isostatic Pressing (HIP) is widely used as a post-processing heat treatment for LPBF components [26]. By applying high temperature and pressure simultaneously, HIP can significantly reduce internal porosity and improve the overall grain structure of the material [25 - 27]. However, the elevated temperatures involved in HIP can lead to surface oxidation when residual oxygen is present in the furnace atmosphere. In titanium alloys, this results in the formation of an oxidized surface layer known as the "alpha case," which is characterized by a high concentration of alpha-phase grains [28, 29]. This brittle surface layer is highly susceptible to the initiation of microcracks, which are especially detrimental to the fatigue performance of titanium components [29].

2.2 Surface Texture of LPBF Components

An additional challenge in the production of engineering components by LPBF is the formation of a surface layer composed of partially melted and sintered powder particles. While surface texture can be moderately influenced by process parameters [7, 30], the resulting high

surface roughness remains a significant drawback, adversely affecting part quality and mechanical properties [5, 31, 32]. Consequently, for components that are subject to cyclic loading or are designated as stress-critical, post-processing treatments aimed at improving surface finish are essential to ensure structural integrity and long-term reliability. Complicating this issue is the fact that surface texture varies significantly based on the part geometry and its orientation relative to the build plane [6, 20, 24]. This variability presents challenges for surface characterization, as demonstrated by Cabenettes et al. [31], who conducted a detailed analysis of LPBF surfaces. Their study assessed the effectiveness of various surface roughness metrics in capturing surface quality and differentiating the effects of build orientation. Notably, the wide range of surface orientations within a single build can influence the efficacy of post-processing techniques aimed at improving surface finish [24 ,31].

Regarding the build process in LPBF and resulting surface texture, there are three primary surface orientations to consider. vertical surfaces are orthogonal to the build plane and have no inclination relative to the incident laser. upskin surfaces are inclined upward toward the laser and are supported by previously solidified material beneath; these surfaces generally exhibit less partially melted powder [7, 23]. In contrast, downskin surfaces are inclined downward toward the build plate, adjacent to loose powder and unsupported by prior solidified layers. This orientation often results in higher levels of adhered or sintered powder on the surface [23, 32].

Another factor affecting surface topography is the “stair-stepping” effect, which arises from the layer-wise nature of the process [23, 32]. However, this effect may be obscured by the accumulation of partially melted powder. vertically oriented surfaces typically exhibit intermediate characteristics, lacking the staircase geometry but still exhibiting some powder adhesion. As a result, LPBF components often display substantial variation in surface

morphology across different regions, and any evaluation of post-processing methods must account for this diversity.

2.3 Post-Processing of LPBF Components

Post-processing surface treatments are critical for enhancing the performance of titanium components produced via LPBF, particularly for applications in aerospace where surface roughness, residual stress, and oxide contamination can negatively impact fatigue life [33, 34]. Chemical milling is currently the industry standard for surface finishing and alpha case removal in Ti6Al4V components [12, 35]. It can be used to reduce roughness and removal of partially melted particles. Chemical milling also effectively eliminates the brittle, oxygen-enriched alpha case formed during high-temperature treatments [35]. However, the process relies on aggressive chemical etchants, raising significant environmental and health concerns [36]. Additionally, chemical milling does not introduce compressive residual stresses due to the absence of deformation or appreciable heat, which are capable of enhancing the fatigue resistance of metallic parts [12].

In contrast, shot peening is widely used for inducing compressive residual stress and improving fatigue life. However, shot peening requires direct line-of-sight to the surface, limiting its ability to treat complex geometries such as internal channels or surfaces with steep inclination, which are common features in AM components [11 - 13, 37]. To address these limitations, alternative “shotless” peening techniques have been investigated. Water jet peening (WJP) and its derivative, abrasive waterjet peening (AWJP)**,** use high-pressure water or slurry streams to generate plastic deformation without the use of solid shot particles [12, 13, 38-41]. Cavitation peening, which uses the implosion of vapor bubbles generated by cavitating jets,

lasers, or ultrasonic waves, also shows promise for introducing residual stress and enhancing fatigue strength [42, 43].

2.4 Cavitation Surface Treatments

A novel technique among those that rely on cavitation, CASF combines the benefits of surface smoothing and the introduction of residual stress. In CASF, a high velocity cavitating jet is injected into an abrasive slurry tank, creating a bubble cloud that accelerates abrasive particles toward the component surface. This dual-action process removes surface irregularities (i.e. causing a reduction in the roughness) and imposes compressive residual stress through localized plastic deformation caused by bubble collapse [13, 14]. Notably, CASF does not require direct line-of-sight, making it particularly well-suited for complex geometries with internal features. The process is also environmentally benign, utilizing only water and inert abrasives. Early investigations suggest that CASF may be effective in simultaneously removing alpha case layers, smoothing rough surfaces, and introducing residual stress, making it a strong candidate for post-processing of LPBF titanium components that are intended for cyclic loading conditions [13, 14].

Several alternative peening techniques are used for surface treatment. Water Jet Peening (WJP) and its variant, Abrasive Waterjet Peening (AWJP), are notable examples [12,13, 41- 43]. Another method, Cavitation Peening (CP), uses a cavitating jet of water to impact the surface through the implosion of vapor bubbles but lacks the abrasive slurry that CASF utilizes. There are also variants of cavitation peening that use a pulsed laser to generate cavitation bubbles [12, 44]. While these alternative cavitation techniques can introduce compressive residual stress and enhance the fatigue strength of metallic components, without the mass of a shot media to transfer

kinetic energy into inelastic distortion the shotless techniques are not effective at reducing surface roughness as other shot based surface finishing techniques [12].

2.5 Summary

To date, no comprehensive study has been conducted on the residual stresses induced by Cavitation Abrasive Surface Finishing (CASF) in Ti6Al4V components. This represents a critical knowledge gap, as understanding and controlling residual stress is essential for optimizing mechanical performance, particularly fatigue strength, in aerospace and biomedical applications. Addressing this gap is necessary to advance CASF along the Technology Readiness Level (TRL) scale and support its adoption as a viable post-processing method for titanium alloy components produced by additive manufacturing.

Chapter 3. Methods and Materials

3.1 Materials

All test coupons used in this study were fabricated using Ti6Al4V titanium powder and an EOS M290 laser powder bed fusion system (EOS, Krailing, Germany). The powder was in a reused state, having been utilized in an unknown number of previous builds. As such, specific information regarding the number of reuse cycles, vendor details, or prior exposure duration was not available. Despite this, the powder met the specifications outlined in ASTM F2924 [45].

The printed samples consisted of rectangular coupons measuring 25 mm in width, 50 mm in length, and with thicknesses of 2, 4, and 6 mm. Half of the plates were printed in a vertical orientation, aligned parallel to the XZ plane as defined by ASTM 52921 [46]. The remaining plates were printed at a 45° tilt relative to the XZ plane. The samples printed with 45° orientation resulted in both the upskin and downskin surfaces having the same orientation as the vertical side surfaces. All samples were fabricated using the manufacturer's default print parameters for Ti6Al4V, as recommended for the EOS M290 system. Wrought specimens of Ti6Al4V were used as a control target with the same dimensions as those produced by LPBF. They were included to provide a surface that started free of defects and had minimal roughness.

In addition to the flat plat samples used for surface treatment studies, hexagonal bars were provided for this investigation by our industry partner Boeing Additive Manufacturing (BAM). These bars were printed on an identical EOS M290 printer with the same default printing parameters. After completion of printing, the bars were removed from the build plate and subjected to a Hot Isostatic Pressing (HIP) process conducted by a commercial vendor

located in the US (name withheld). The HIP treatment was performed at a pressure of 190 MPa and a temperature of 815°C for a duration of two hours. During the process, four of the bars were exposed to oxygen, resulting in the formation of an oxide layer on their surfaces. The oxide layer is referred to as an alpha case in this investigation.

3.2 Equipment

All coupons printed at the University of Washington were subjected to a stress relief heat treatment of 745 ˚C for 2 hours before being removed from the build plate by bandsaw. After they were stress relieved, the coupons were sectioned from the build plate with a horizontal bandsaw. The coupons were then shipped to our partner Sugino corporation (Toyama, Japan) to be treated with the novel CASF treatment. All coupons received different treatment parameter combinations.

3.3 Build Designs

This investigation primarily focused on samples produced in two separate builds as shown in Figure 3.1. Each build was designed to achieve a part geometry that could be produced through LPBF and that was a relevant target for the treatment process. Each style of coupon isolated one quality that a surface could exhibit in its design, focusing primarily on sheet thickness and orientation of build direction.

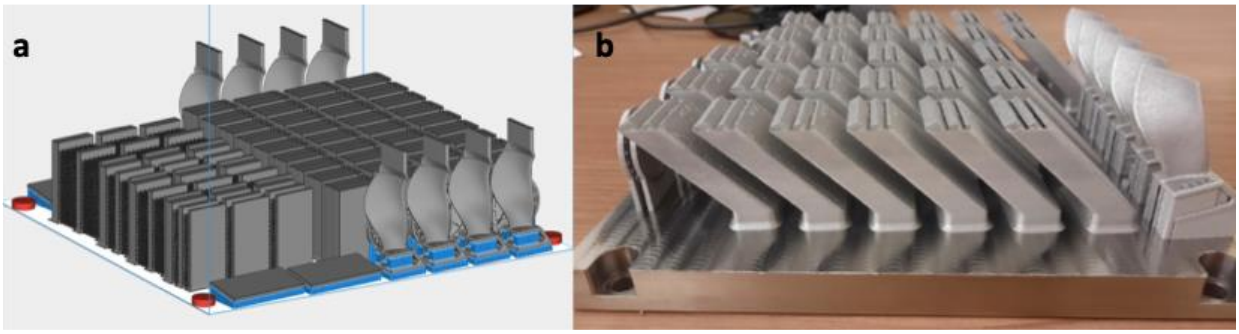

Figure 3.1 LPBF builds for this research. a) 3D rendering of Build 1, and b) Build 2 prior to being removed from the build plate.

The goal of Build 1 (Figure Figure 3.1a) was to produce a set of standard vertically printed plate coupons for evaluating the effects of CASF treatment on the surface roughness, residual stress, geometric distortion, and material removal. The coupons were printed with thicknesses of 2, 4, and 6 mm with range that enabled the distortion of the metal to be controlled.

The primary goal of Build 2 (Figure 3.1 b) was to generate characteristic upskin and downskin surfaces on flat plate coupons to evaluate the efficacy of CASF treatments on these surfaces relative to the vertical build orientations. The coupons were printed at 45˚ from the build plate, which results in greater roughness from that of the vertical orientation due to a "stair stepping" effect from the layered printing process as well as from increased un-melted particles remaining on the surface of the part.

An extra set of specimens were provided by Boeing as an additional challenge for the CASF treatment process. These specimens consisted of eight identical hexagonal bars with width and length of approximately 2cm x 10cm respectively. The hex bars were subjected to Hot Isostatic Pressing as a postprocessing treatment and four of the eight bars had developed a layer of alpha case from this treatment. These specimens serve as an opportunity to test the ability of CASF to

remove the embrittled alpha case, and to measure the effectiveness of CASF on surfaces that do not receive direct line of sight treatment.

3.4 CASF Treatment Parameters

The CASF treatment process involves several process parameters. Based on results from prior applications, Sugino isolated the traverse rate of the nozzle as the parameter with greatest impact on the CASF treatment [14].

The CASF treatment of the flat coupons from Builds 1 and 2 consisted of a raster pattern with 4 mm offset between each traverse pass and 8 linear passes in total across the width of the plates. For every pass, the nozzle operated at a standoff distance of 50 mm from the surface of the sample. A water pressure of 150 MPa was applied while the nozzle rotated at 200 revolutions per minute to create a symmetric cavitation cloud. The traverse speed varied for all the experiments from stationary dwell treatment to a traverse speed high as 120 mm/min.

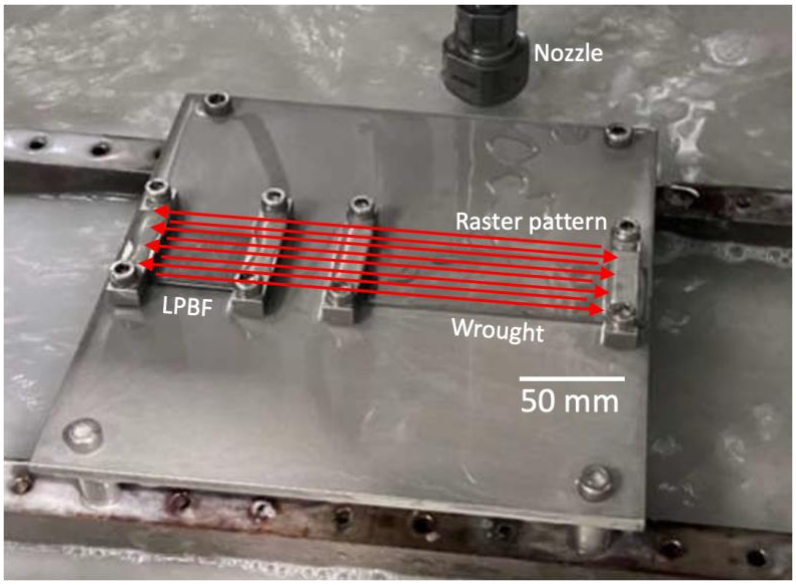

Figure 3.2 The CASF tool path for treatment of a set of coupons. The coupon on the left labeled "LPBF" is from Build 1 and the coupon on the right labeled "Wrought" is from a sheet of Ti6Al4V used as a control.

An alternative treatment was also performed on the plates of Build 1 with the nozzle positioned at a 45-degree angle to the plate surface as shown in Figure 3.3. This treatment served as an opportunity to examine the effectiveness of CASF with impingement angles that are not orthogonal to the target.

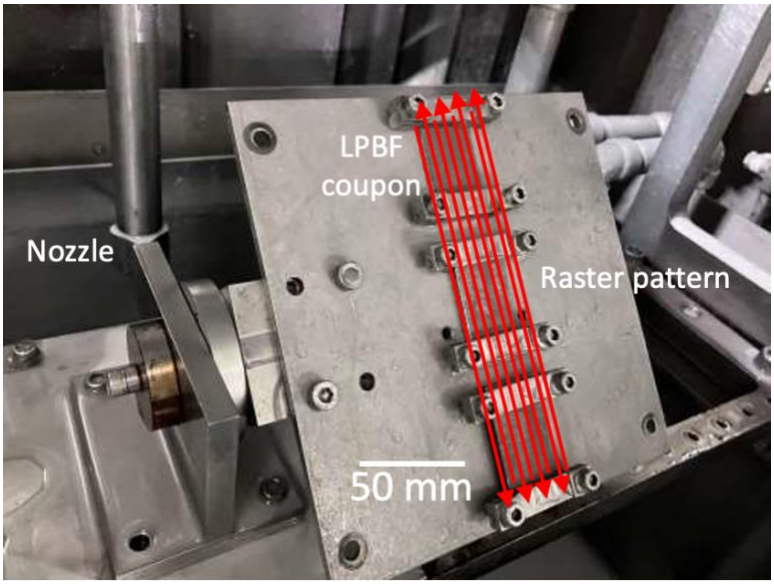

Figure 3.3 CASF tool path used for treating printed coupons from Build 1 at a 45˚ angle from the target surface.

3.5 Residual Stress Analysis

The residual stress in the treated surface of the Ti6Al4V samples was estimated using the $\sin^2(\psi)$ method [47]. X-Ray diffraction was performed using a Bruker D8 Discover X-ray Diffractometer (XRD) (Bruker, Billerica, MA) and with a copper target (Cu Kα) used for the X-Ray source. The XRD generated X-Rays at 50 kV and 1000 μA and focused the beam using a 0.5 mm collimator. A Pilatus 100K large area 2D detector was used to capture diffracted photons from the [312] plane at $2\theta = 110^{\circ}$. The diffraction pattern was measured at nine distinct orientations for

each sample with a full complement of Φ (0˚, 45˚, and 90˚) and ψ (0˚, 22.5˚, and 45˚) combinations. The scans were performed with a 2D detector capturing a 2θ range from 107˚ to 113˚, which resulted in a total elapsed time of 4 minutes per scan [48]. The residual stress in the metal was estimated from the location of the diffraction peaks at these angles using Bruker's software (Bruker, Diffrac.Leptos7, Billerica, MA). The location of each peak was evaluated using a standard gravity method using the 5 outside data points on each side of the peak to define and then filter out the background level. Each diffraction peak was then weighted using a least squares regression such that the weight assigned to each peak was proportional to the diffraction intensity.

The $\mathrm{Sin}^2(\psi)$ method involves measuring the 2θ position of a single diffraction peak at multiple orientations of phi and psi angle combinations (Φ, ψ), and measuring the peak shift with respect to the diffraction pattern for the stress-free condition. The residual strain can be calculated by relating the change in lattice spacing indicated by the peak shift according to Bragg's Law. Peak broadening also often occurs in deformation processes due to the non-uniformity in micro strains within the crystals over the depth of x-ray penetration. The orientation specific strain at any (Φ, ψ) can be related to the volumetric strain through the tensor product in Equation 3.1,

$$\varepsilon_{\Phi\psi} = \varepsilon_{ij} * h_i^{\Phi\psi} * h_j^{\Phi\psi} \tag{3.1}$$

which can then be expanded into Equation 3.2 for a rectangular coordinate system [48]

$$\varepsilon_{\Phi\psi} = \varepsilon_{11}\cos^2(\Phi)\sin^2(\psi) + \varepsilon_{12}\sin(2\Phi)\sin^2(\psi) + \varepsilon_{22}\sin^2(\Phi)\sin^2(\psi) + \varepsilon_{13}\cos(\Phi)\,sin(2\psi) + \varepsilon_{23}\sin(\Phi)\,sin(2\psi) + \varepsilon_{33}\cos^2(\psi) \tag{3.2}$$

Once the cartesian strain distribution is calculated, the next step is to utilize the strain to estimate the stress according to generalized Hooke's Law. The strain vector described by Equation 3.2 is related to the stress tensor according to Equation 3.3.

$$\varepsilon_{\Phi\psi}^{hkl} = S_1^{hkl}(\sigma_{11} + \sigma_{22}) + \frac{1}{2}S_2^{hkl}(\sigma_\Phi)(\psi) \tag{3.3}$$

where S_1 and S_2 are defined in Equations 3.4 and 3.5.

$$S_1^{hkl} = -\frac{v}{E} \tag{3.4}$$

$$S_2^{hkl} = \frac{2(1+v)}{E} \tag{3.5}$$

Note that the superscript hkl is retained to reflect the fact that the Young's modulus and Poisson's ratio are not consistently isotropic on the micro length scales and are different for different crystal planes. However, for an assumption of equi-biaxial plane stress, i.e., when σ_3=0, Equation 3.3 can be further simplified to Equation 3.6.

$$\varepsilon_{\Phi\psi}^{hkl} = S_1^{hkl}(\sigma_{11} + \sigma_{22}) \tag{3.6}$$

3.6 Sub-Surface Stress Analysis

To understand the sub-surface stress distribution resulting from the CASF treatment on the titanium samples, a series of sequential surface measurements were conducted after prescribed levels of material removal. Specifically, incremental layers of material were removed by etching using Kroll's Reagent (etchant #192 of ASTM E407- 07) [49]. To restrict material removal to the area of interest, an acrylic-based nail polish was applied to the top surface of the metal to act as a mask and outlining the perimeter. Then, Kroll's reagent was applied to the unmasked surface for periods up to five minutes at room temperature. A commercial digital micrometer with a resolution of 0.00005 in and flat anvils (SHARS Tool, St. Charles, IL) was used to quantify the thickness of the sample after etching and to support estimating the corresponding material removed. This process consisted of measuring the total thickness of the coupon before and after the etching increment and calculating the difference in thickness. Between 5 and 10 μm of material removal

was targeted between successive XRD scans to achieve measurements with adequate spacing to define the gradient of stress as a function of depth into the material.

3.7 Profilometry

Profilometry was performed to characterize the surface roughness of the samples before and after treatment by CASF. A Keyence VR-3100 optical profilometer (Keyence America, Itasca IL) was used to conduct areal scans that enabled roughness profile measurements. The profiles were obtained perpendicular to the lay, which was defined by the build layers. The Keyence used a multi-line roughness technique averaging the roughness of five lines. A cutoff length λ_c of 2.5 mm was used with five cut off lengths being measured in each line. Each line had a total traverse length of 17.5mm with the outer most traverse lengths being filtered out. These parameters were chosen to conform to the ISO 4288 standard [50] for surface texture.

3.8 SEM Imaging

Scanning electron microscopy (SEM) was used to evaluate the changes in surface morphology of the samples resulting from the CASF treatment. An Apreo-S SEM (ThermoFisher Scientific, Waltham, MA, USA) was used for imaging. The images were taken of samples over a variety of magnification and without any sputter coating. All images were taken at a working distance between 5 and 12 mm with at voltage and current values of 25 kV and 3.2 nA, respectively.

3.9 Optical Imaging

To characterize contributions to the changes in surface texture resulting from CASF, cross sections of the treated coupons were prepared for optical imaging. The cross sections were mounted in black glass-filled epoxy (Allied 150-10105, Cerritos, CA) in cylindrical molds. The

exposed surfaces were then polished using silicon carbide abrasive mesh pads from #240 to #800 mesh (Allied 50 series, Cerritos, CA). Thereafter, a final abrasive polish was performed using a 9 μm DiaLube diamond particle suspensions on a Struers MD-Dac pad (Struers, Cleveland, OH), followed by a chemical attack polish on a Struers MD-Chem pad with a solution comprised of 10 ml 0.05 μm colloidal silica, 0.5 ml 5% ammonium hydroxide, and a few drops of 40% hydrogen peroxide. Optical images were obtained from these treated surfaces using an Olympus BX51M optical microscope (Center Valley, PA USA) at between 5X and 50X magnification.

Chapter 4. RESULTS

The effectiveness of the CASF treatments to reduce surface defects and introduce compressive residual stress were measured with scanning electron microscopy, optical microscopy, x-ray diffraction, and profilometry.

4.1 Scanning Electron microscope

Representative SEM images of the LPBF samples before and after CASF treatment are shown in Figure 4.1. Specifically, the printed metal with vertical, upskin, and downskin orientations is shown in Figure 4.1(a,c), 4.1(b,d) and 4.1 (c,e), respectively.

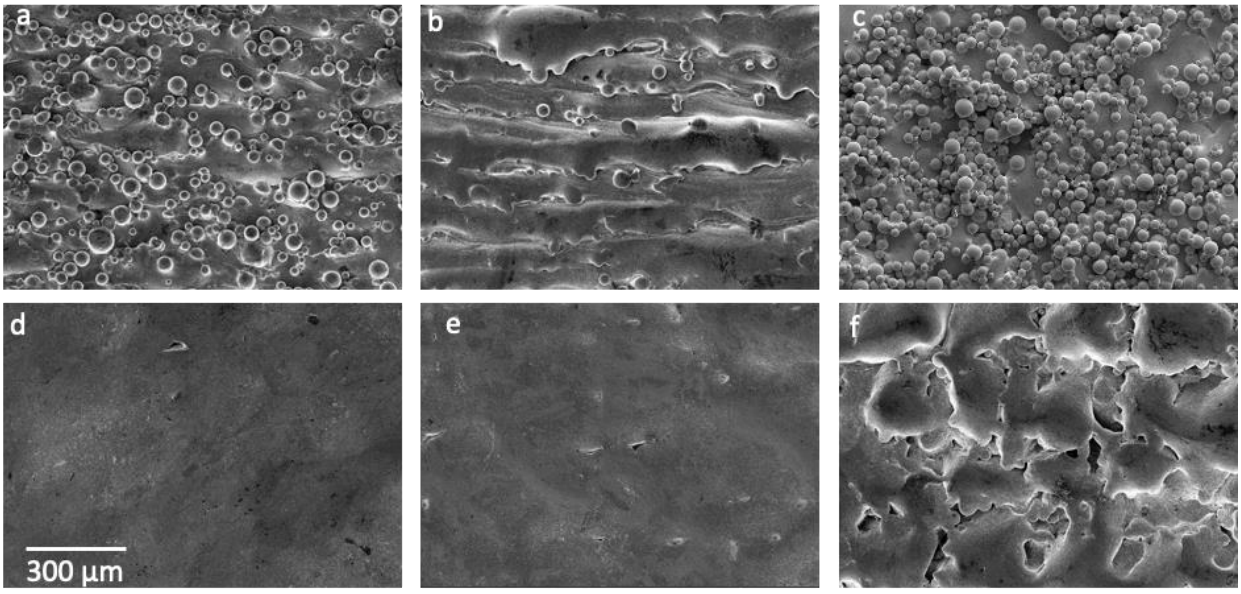

Figure 4.1 SEM images of the Ti6Al4V samples. a-c show the as-built condition in the vertical, upskin, and downskin build orientations, respectively. Similarly, d-f show the CASF treated condition in the vertical, upskin, and downskin build orientations after treatment at 80 mm/min. The build direction for all images is vertical relative to the page and the scale bar applies to all pictures.

As evident from Figure 4.1, CASF removed the partially sintered powder particles from the parent metal surface for all three build orientations. In the upskin and vertically printed samples, this resulted in significant improvements in surface roughness and the elimination of surface defects. However, in the downskin orientation it appears that some unconsolidated metal has become exposed, which is evident after powder removal. These features are more likely for downskin layers as they are formed over a bed of loose powder, leading to incomplete fusion. At a feed rate of 80 millimeters per minute, the CASF treatment appears unable to remove this partially fused layer to reach a depth of fully dense base metal.

4.2 Optical Micrography

To obtain a complimentary perspective of the treatment effectiveness, cross sections of the three sample orientations were cut and etched to reveal the surface morphology and expose the underlying grain structure. Figure 4. shows a detailed view of the surface of metal printed vertically with LPBF in the as-built condition, before and after CASF treatment.

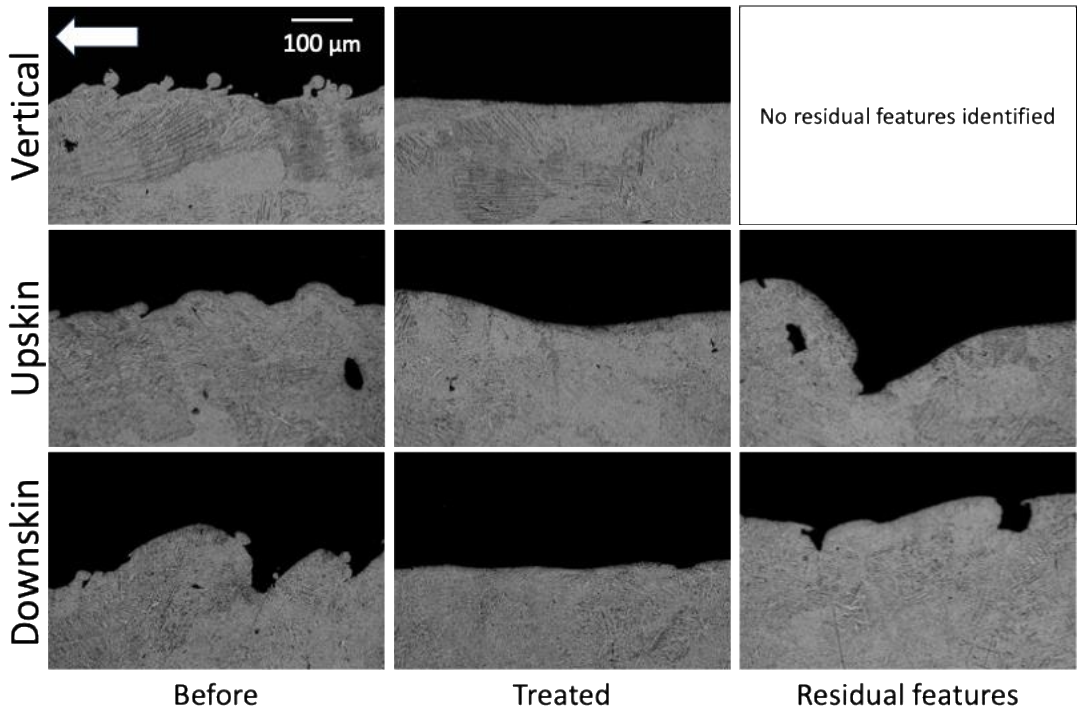

Figure 4.2 Comparison of vertical, upskin, and downskin printed metal in the as-built and CASF treated conditions. Residual features that were identified on the upskin and downskin treated metal are also shown.

In Figure 4.2, the first column shows the untreated surfaces in the as-built condition. Powder particles fused to the parent metal can be identified on all three surfaces, especially on the vertical surface. In the cross section, the particles appear as spheres that are attached to the bulk metal by narrow bridges of metal or sinter-necks. The as-built surfaces exhibit rough profiles for all three surface orientations; the downskin surface exhibits the most distinct stair stepping effect.

The second column of Figure 4. presents representative views of the "Treated" condition and reflects the majority of the surface that was evaluated under the microscope. Not only is the powder removed from the surface; it can also be observed that the underlying roughness is improved by the CASF treatment.

The third column in Figure 4.2 presents "Residual features" of the treated surfaces, including valleys that were not fully treated by CASF. These valleys appear to be consistent with

the features identified on the surface of the treated samples in Figure 4.(d) and 4.1(e), which appear as pockets on the surface. However, these residual features were relatively uncommon, occurring in only 10% or less of the observed surface.

4.3 Residual Stress

Due to the importance of surface residual stresses to the fatigue response of metal components, measuring the compressive residual stress imparted by CASF was a primary objective. In addition, measurement of the residual stress enabled comparison of CASF to other surface treatments including chemical milling and various peening methods [12, 13, 51].

Based on the novelty of the CASF process and the limited understanding of the jet structure in terms of the distribution of cavitation bubbles and abrasive particles, it was considered necessary to begin by mapping the residual stress in terms of distance from the jet center. This process enabled measurement of the effective treatment area achieved by a single treatment pass across the surface. Briefly, a spot treatment was conducted such that the CASF nozzle was held stationary over the specimen without traverse for an elapsed time of 6 minutes. The treatment pattern consisted of highest treatment intensity in the center and decreasing treatment intensity extending radially away from the center. Performing spot treatments in this manner enabled residual stress measurements to be conducted radially away from the center of the crater to describe the effective treatment area achieved in terms of both surface texture and residual stress. Figure 4. presents results of these measurements.

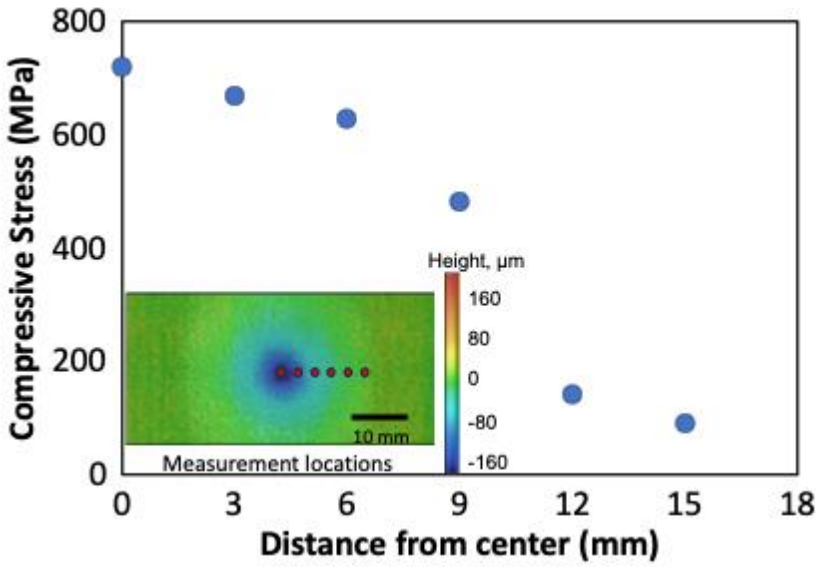

Figure 4.3 Measurements of residual stress from spot treatment indicated from the center outward for a 6 minute CASF dwell on vertically printed metal.

The profile presented in Figure 4. suggests that the CASF cloud has a "primary radius" of effective treatment between 6 and 9 millimeters from the center of the jet. Beyond that distance there is a sharp decrease in residual stress magnitude with close to no treatment beyond 12 millimeters. The results in Figure 4.3 provide confidence that the treatment offset of 4 mm between traverse paths ensured complete and uniform treatment of the target.

To assess the surface treatment applied over a target area that requires sequential passes, the compressive residual stress was measured on the plate samples treated by CASF over feed rates that ranged from 20 to 120 mm/min. Results of this effort applied to the plate samples with 6 mm thickness that were printed vertically by LPBF are shown in Figure 4..

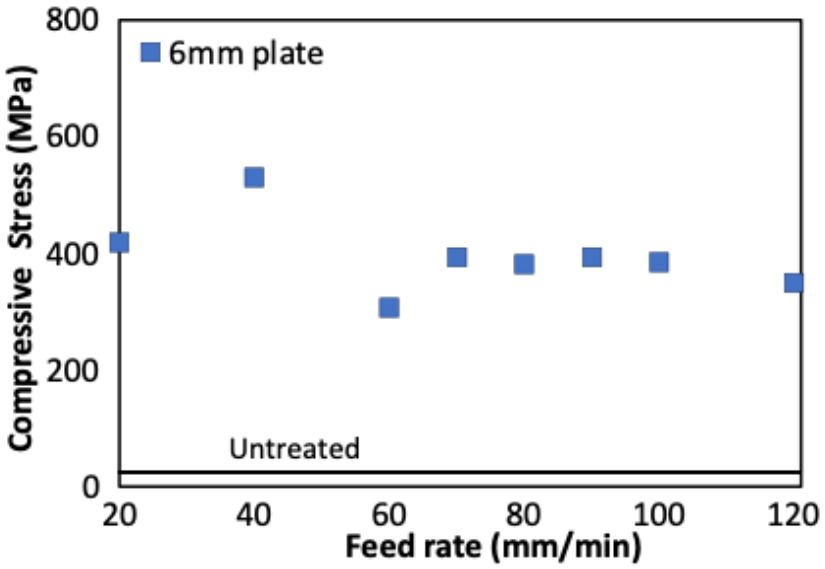

Figure 4.4 Compressive residual stress on 6 mm thick plates after treatment by CASF. Feed rates ranged between 20 and 120 mm/min. The residual stress of the as-built condition is also shown for comparison.

While there is some variation between samples. There is no discernable dependance of residual stress on feed rate. The overall average compressive residual stress resulting from the CASF treatment is 390 ± 40 MPa.

In addition to evaluating the effect of treatment feed rate for the vertical orientation, the residual stress within metal targets with upskin and downskin printing orientations were also evaluated. Figure 4.5 presents a comparison of the residual stress for feed rates ranging from 60 to 120 millimeters per minute for vertical, upskin, and downskin printed specimens with a 6 millimeter thickness.

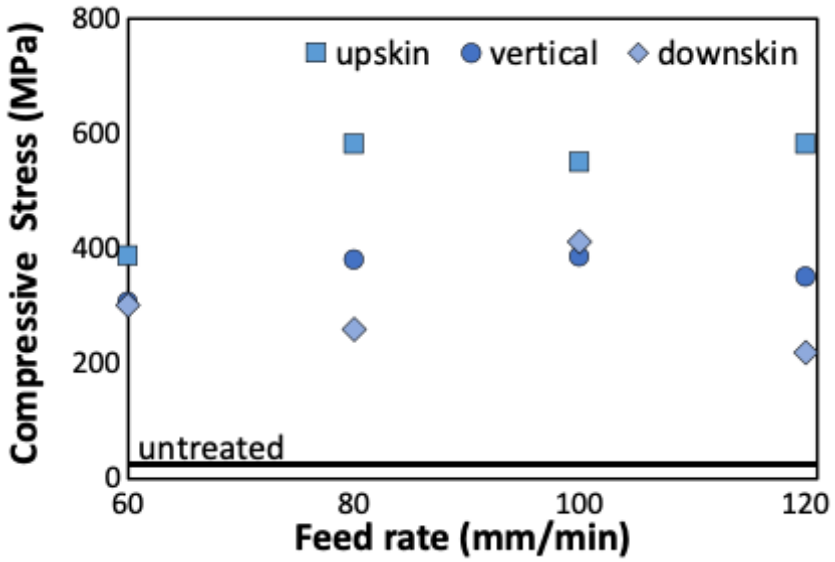

Figure 4.2 Surface residual stress of the Ti6Al4V samples with upskin, downskin, and vertical printing orientations treated with CASF. The untreated condition residual stress is shown for reference. All samples have a thickness of 6 millimeters.

Similar to Figure 4.4, there is no apparent influence of feed rate on the magnitude of residual stress over the parameter range evaluated. However, printed surface orientation is very important. The overall average compressive residual stress resulting from treatment of the vertical, upskin and downskin orientations is 355 ± 36, 524 ± 93 and 297 ± 83 MPa, respectively, which are significantly different ($p = 0.0053$). It is important to note that the upskin treated surfaces achieved higher magnitude compressive residual stress that in the vertical and downskin specimens at the same feed rates. Based on the surface morphology of the as-built condition in Figure 4.1, it appears that the CASF process can introduce a greater residual stress in metal with less residual powder coverage. The upskin surfaces were consistently noted to have less un-melted powder covering the surface prior to treatment, which can be observed in Figure 4.. While this is a plausible

interpretation of why the downskin metal has lower residual stress, it is also possible that the larger number of residual valleys evident of this surface orientation result in stress relief that limits the residual stress.

In addition to examining the effect of LPBF build direction on the CASF treatment effectiveness, the effect of treatment orientation relative to the target surface was also evaluated. For this effort the target surfaces were arranged at a 45˚angle from the CASF nozzle axis. Figure 4. compares the residual stress resulting from treatments performed with jet oriented perpendicular and 45˚ to vertically printed 6 mm thick specimens over feed rates ranging from 60 to 120 mm/min.

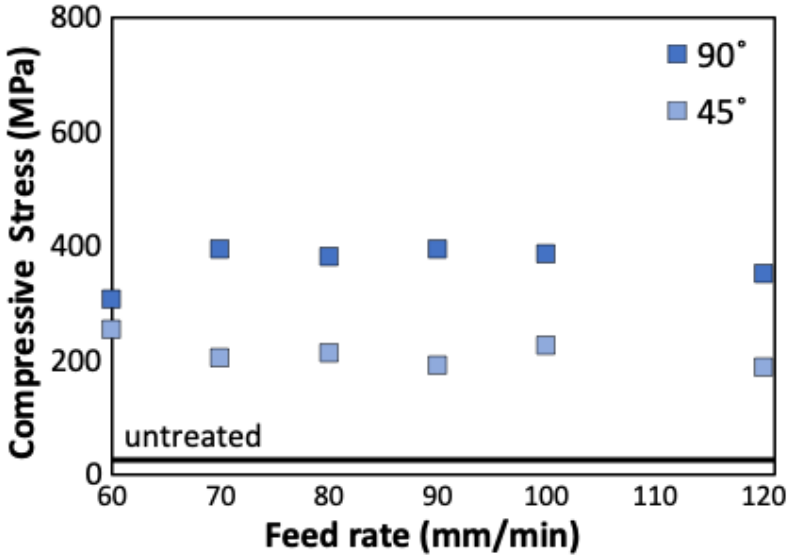

Figure 4.6 Effect of surface orientation on residual stress of CASF treated samples. Treatments were performed at impingement angles of 90˚ and 45˚.

As evident in this figure, the 45˚ treatment orientation resulted in lower magnitude of residual stress compared to orthogonal treatment, as expected. There was no discernable trend in the residual stress with feed rate. The overall average compressive residual stress in the plate

samples treated with 90° and 45° orientations are 368 ± 34 and 211 ± 25 MPa, respectively. These measures are significantly different ($p \leq 0.05$).

Based on the results of prior work it became clear that an analysis of the depth of residual stress was needed to further understand the CASF treatment effectiveness. Hence, an experiment was conducted to measure the surface residual stress at multiple depths, by the successive etching technique. Residual stress profiles obtained in four separate measurement locations of a 6 mm thick sample treated by CASF at 70 mm/min feed rate is shown in Figure 4..

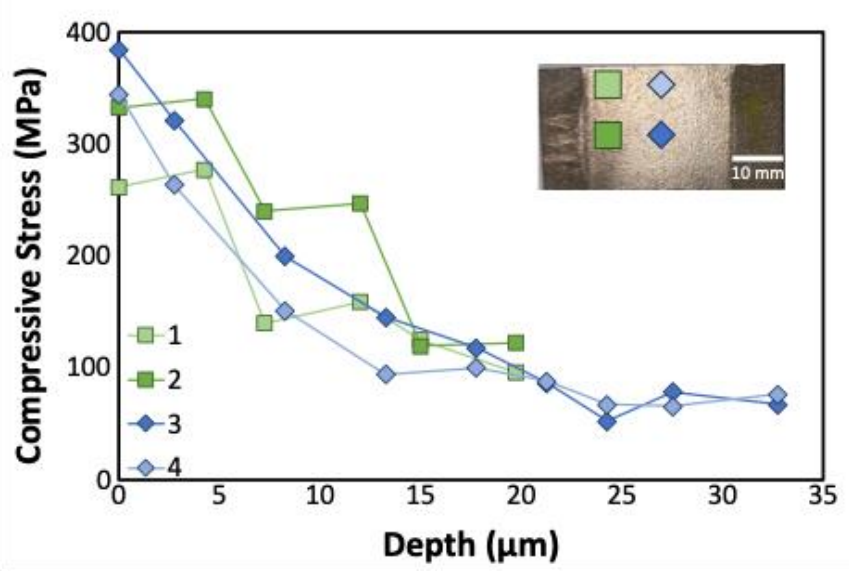

Figure 4.7 Subsurface residual stress distribution for a 6 mm thick sample treated by CASF at 70 mm/min feed rate. Subsequent depths were removed via acid etching.

The subsurface residual stress distribution in Figure 4.7 show that the stress extends about 30 µm from the treated surface before plateauing at approximately 60 MPa. The measurements were taken at four separate locations and all follow the same general trend indicating a consistent treatment along the entire face of the sample. The four locations also appear to show a relationship between residual stress and relative distance from the edge of the coupon; the stress measured at

locations 1 (light shaded green) and 4 (light shaded blue) are consistently 10 - 20% lower than those measured at points 2 (dark shaded green) and 3 (dark shaded blue).

How did the compressive stress of the CASF treatment on LPBF specimens compare to wrought samples that started in a smooth and defect free state? Figure 4.8 shows that while the untreated wrought plates started at a higher untreated residual stress state of 50 MPa the samples ended up with residual stress values of 255 ± 63 MPa which is very similar to the distribution of downskin samples treated with CASF ($p = 0.347$).

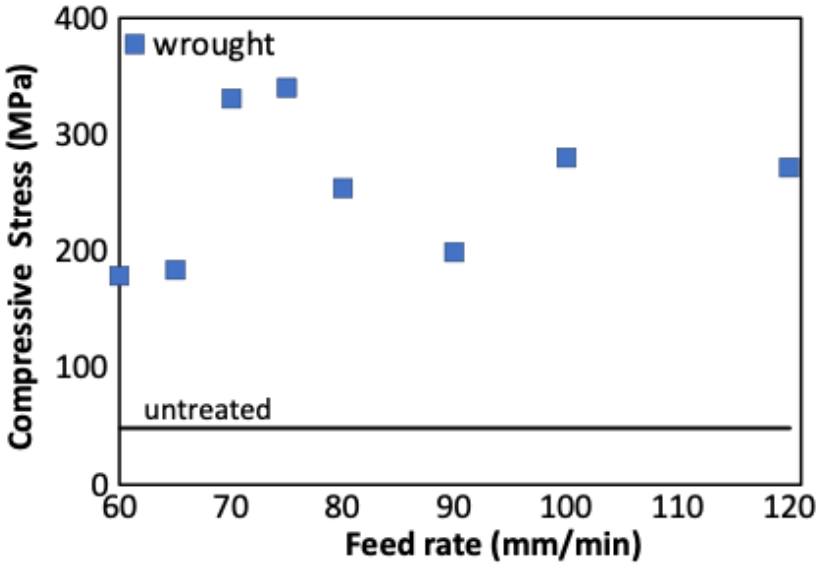

Figure 4.8 Compressive residual stress on 6 mm thick wrought plates after treatment by CASF. Feed rates ranged between 60 and 120 mm/min. The residual stress of the as-built condition is also shown for comparison.

4.4 Roughness

An equally important quality of surface treatments and the fatigue resistance of metal components is the surface texture. In most cases the objective is to achieve a decrease in roughness. For most treated samples the surface roughness was measured along with the residual stress that were obtained from XRD. Interestingly, the results show that the CASF treatments caused a significant decrease in roughness for all conditions, which is expected to increase the resistance to fatigue failure of the LPBF metal [8]. Figure shows the surface roughness as a function of distance from the center of the jet. When comparing results of the roughness measurements to residual stress obtained from the spot treatments, the co-located roughness could only be obtained up to 9 mm away from the center of the jet due to a limitation in available space for profile measurements.

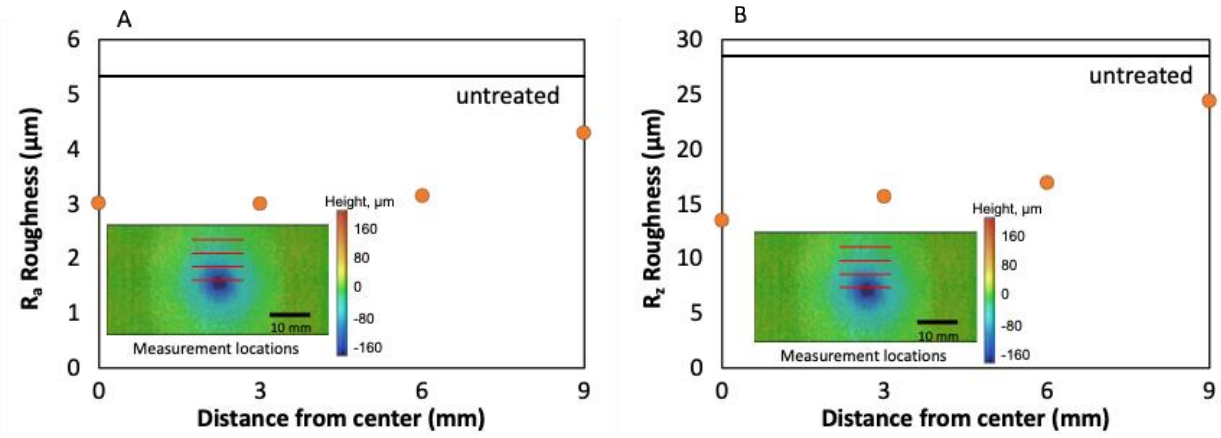

Figure 4.9 surface roughness of CASF spot treatment taken at 3 mm increments radially away from center of treatment. a) average roughness, R_a b) ten-point roughness, R_z.

Similar to the residual stress distribution, the largest degree of improvement in the surface texture occurred in the first 6 mm from the center of the jet; the decrease in treatment effectiveness was more extensive between 6 and 9 millimeters.

Because the build orientation contributed to the surface residual stress as evident in Figure 4.6, it was considered important to assess the effects on surface smoothing of printed metal. Figure

4.(a) and 4.10(b) show the R_a and R_z roughness, respectively, for the metal printed in the vertical, upskin, and downskin orientations.

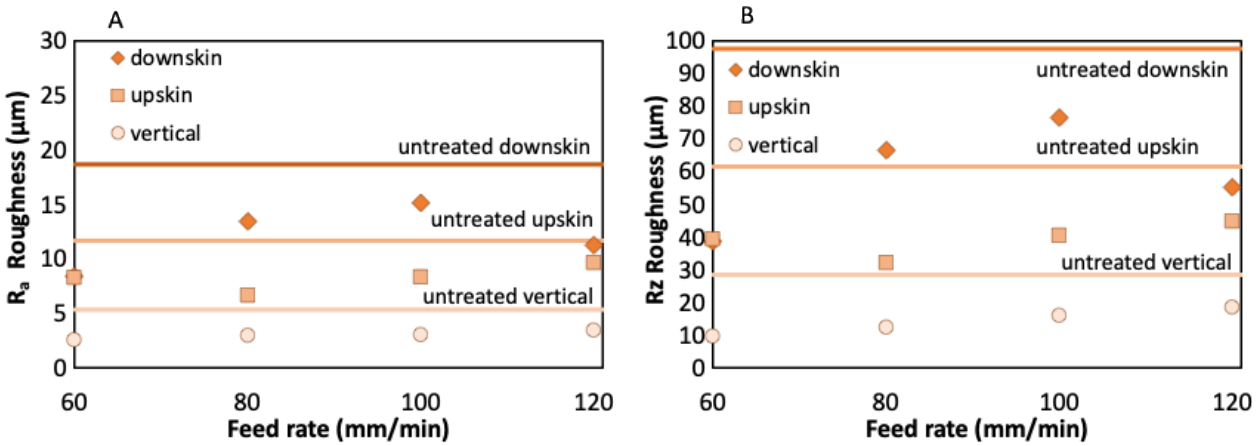

Figure 4.10 Surface roughness of LPBF metal printed with vertical, upskin or downskin orientation and treated by CASF. a) average surface roughness, and b) ten point roughness.

There is a reduction in the surface roughness after CASF treatment for all three orientations and over the entire range of feed rate. The roughness results appear to be consistent with the SEM images in Figure 4., and reflect the comparatively large roughness of the downskin surfaces.

The influence of jet impingement angle on the effectiveness of the CASF treatment was evaluated to complement results regarding the influence of build orientation. Figure 4.3 shows the surface roughness after treatment with impingement orientations of 90˚ and 45˚ angles.

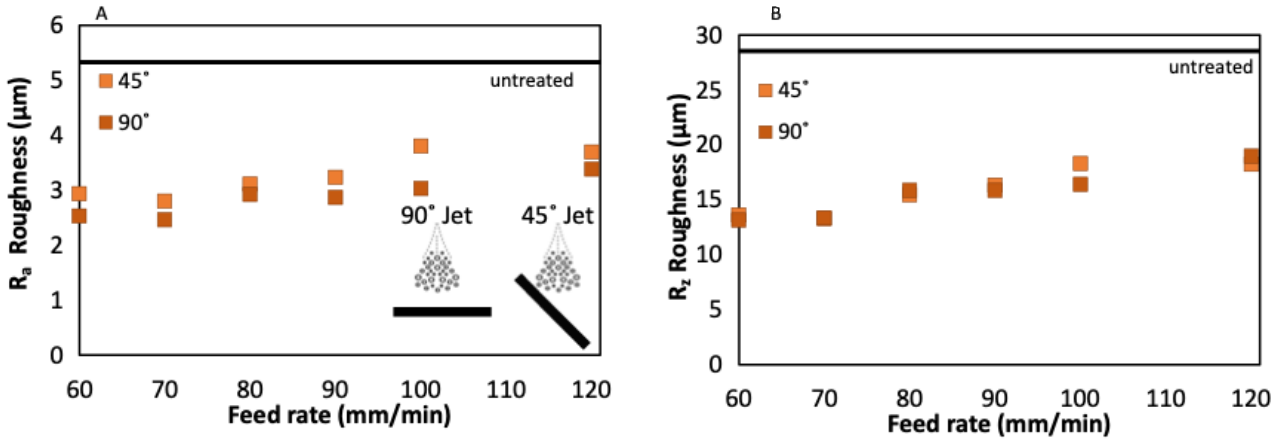

Figure 4.3 Surface roughness of the metal after treatment by CASF at 90˚ and 45˚ angles of impingement. a) average surface roughness, and b) ten point roughness.

Surprisingly, whereas the residual stress was highly dependent on treatment angle and showed significantly lower stress for the 45° treatment, there was no influence of treatment angle on the roughness over the entire range of feed rate explored. This could signify that the physics of smoothing only require a portion of the cavitation cloud to be effective, whereas the residual stress requires direct treatment for the abrasives to impart enough kinetic energy to work harden the metal.

4.5 Hex bar case study

The hex bar samples printed by Boeing provided a unique opportunity to test the effectiveness of CASF in two separate capacities. The first was to evaluate CASF applied to targets without direct line of sight with respect to the nozzle axis. By virtue of the hexagonal cross-section one face was treated directly whereas the five other faces were exposed to treatment at an angle or directly opposed to the line of sight. The second treatment opportunity was to measure the ability of CASF to remove alpha case. The hex bars formed an alpha case during a hot isostatic pressing

treatment though oxygen contamination of the surface. If CASF could remove the alpha case, it could expand the application of the technology.

4.5.1 Residual stress

Figure 4.4 shows the residual stress on four of the six faces of two hex bar samples. One of the sample had an α-case layer of approximately 30 µm thick while the other hex bar did not have an α-case and served as the control. Both samples were treated with CASF on the S1 face at a feed rate of 60 millimeters per minute. Each successive face received an increasingly oblique treatment as indicated in the schematic. The S3 and S4 surface serve as surfaces that do not have line of sight.

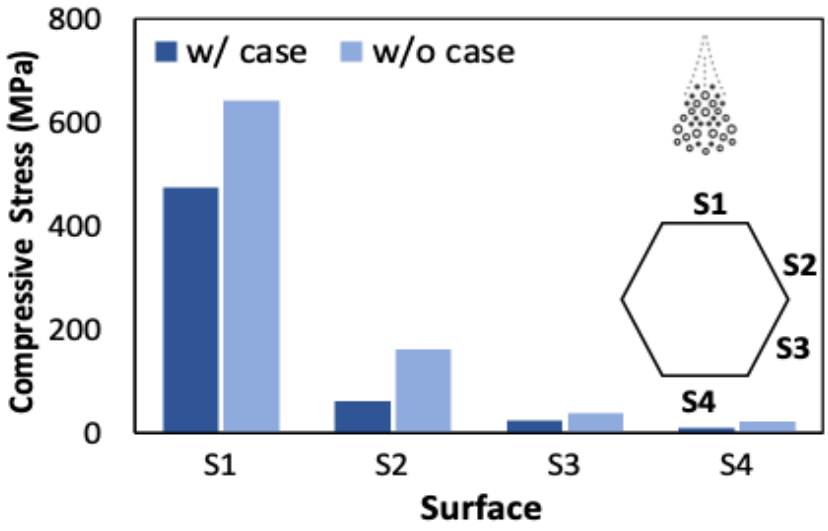

Figure 4.4 Surface residual stress of the various faces of the hexagonal bars with and without an alpha case layer.

As evident in Figure 4.4, the magnitude of residual stress was significantly lower on all faces of the hex bars with alpha case relative to the sample without case. While, the alpha case layer had a significant effect on the residual stress introduced by the CASF treatment, the surface

orientation relative to the jet was the most important factor. Figure 4.12 also shows that although the CASF cloud can treat faces that are oblique to the incident jet (S2), the surfaces directly opposed to the incident jet (S3 and S4) undergo limited changes in surface stress.

Figure 4.5 shows the surface residual stress on the S1 face after CASF treatment over a range in feed rates. Results are shown for the hex bar with alpha case layer and the control. The residual stress shown in this figure is for the top face (S1) only because of the substantial reduction in stress on the other faces. Including the other surfaces would reduce the measurement sensitivity and ability for comparing the treatment effectiveness. Overall, there is no clear trend in the stress for either the hex bar with case or the control over the range in federate examined.

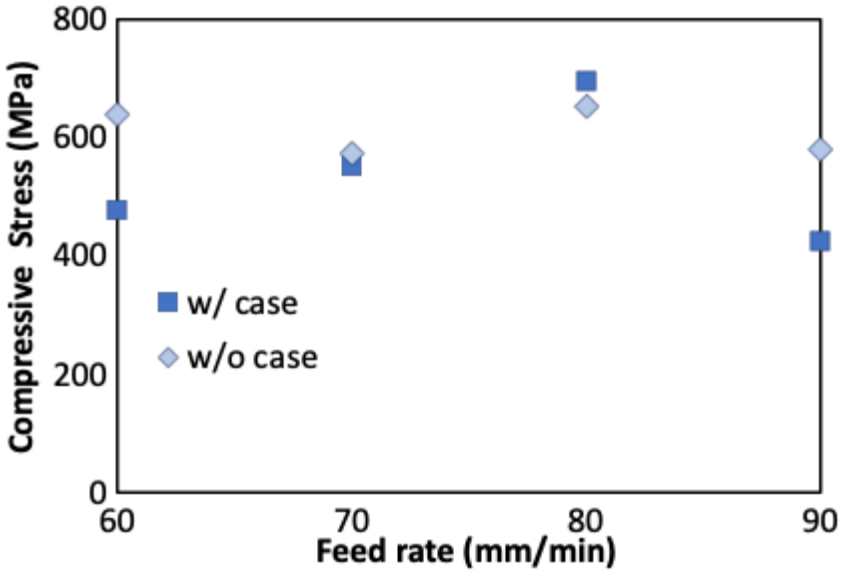

Figure 4.5 Surface residual stress from CASF treatment on the S1 face of hex bars with and without an alpha case over a range in feed rate.

4.5.2 Surface Roughness

Figure 4.14(a) and 4.14(b) presents the average Ra and Rz values, respectively, for the four surfaces of the treated hex bars. The surface texture resulting from CASF treatment of the hex bars

followed similar patterns as the residual stress, i.e. the change in roughness was most substantial on the S1 and S2 faces with significant decrease in effectiveness on the S3 and S4 faces.

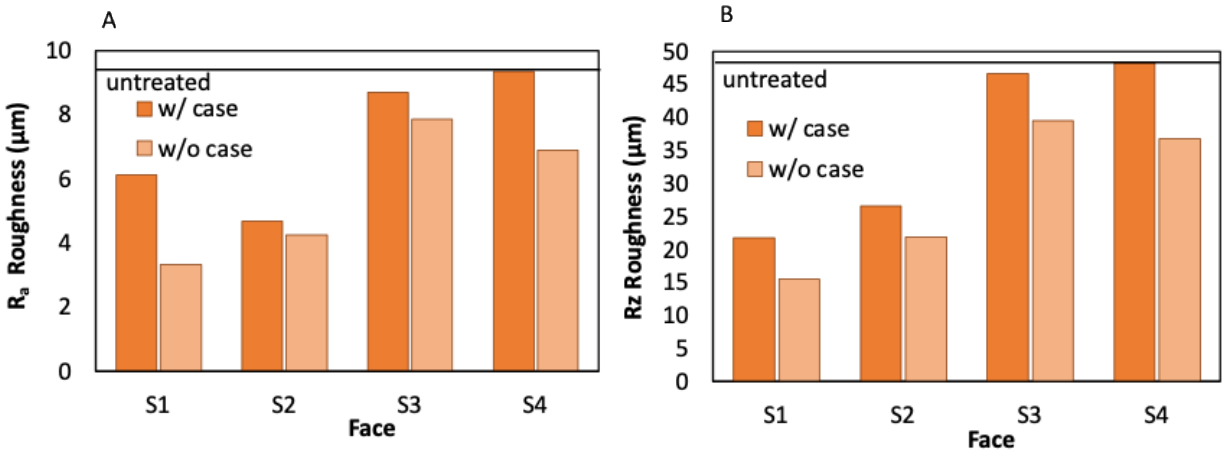

Figure 4.6 Surface roughness of 4 faces of CASF treated LPBF built hex bars. a) average surface roughness, and b) ten point roughness.

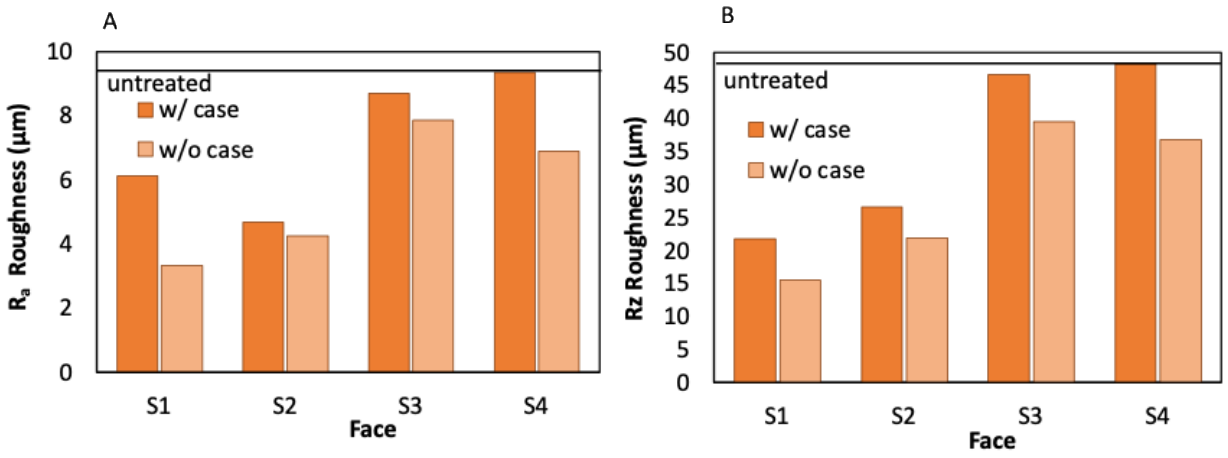

Figure *4.6* shows that the surface roughness was between approximately 20% to 40% higher on all faces of the hex bar with the alpha case than on the control bar without alpha case. There are some differences between the trends in residual stress and surface roughness on the S1 surfaces treated over the range in feed rates, which implies that there is a different component of the CASF process physics that is responsible for the two dependent variables. Whereas the residual stress showed no dependance on the treatment feed rate, the surface roughness did change with the feed rate. As

evident in Figure 4.7, the slower feed rates treatments achieved a greater reduction in surface roughness than those with faster feed rates.

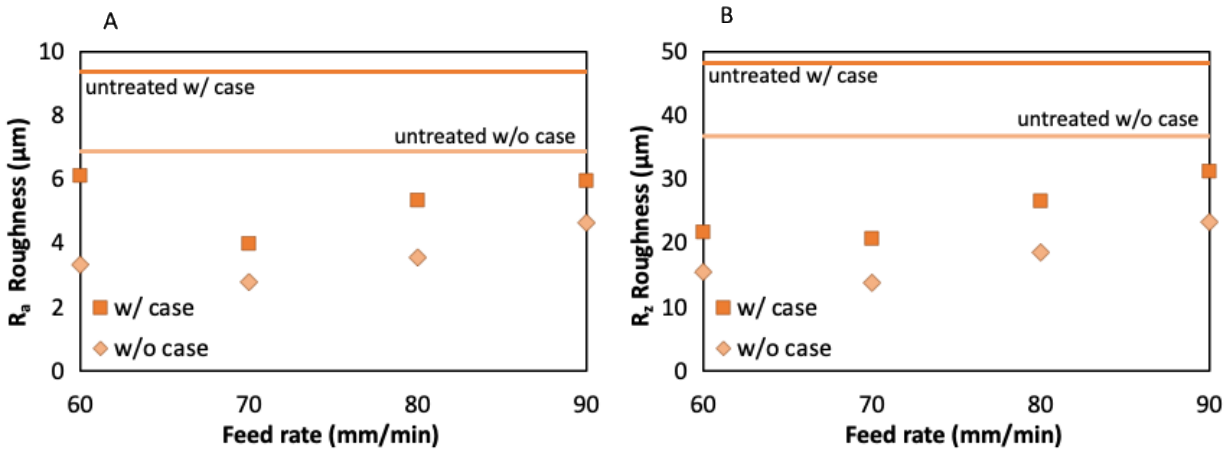

Figure 4.7 Surface roughness of S1 face of hex bar after CASF treatment at various feed rates ranging from 60 to 90 mm/min. a) average surface roughness, and b) ten point roughness.

4.5.3 Alpha case depth

In addition to measuring the residual stress of metal with and without alpha case, the thickness of the alpha case layer on the metal was measured before and after treatment. Figure 4. shows alpha case thickness remaining after treatment over the range in treatment feed rates.

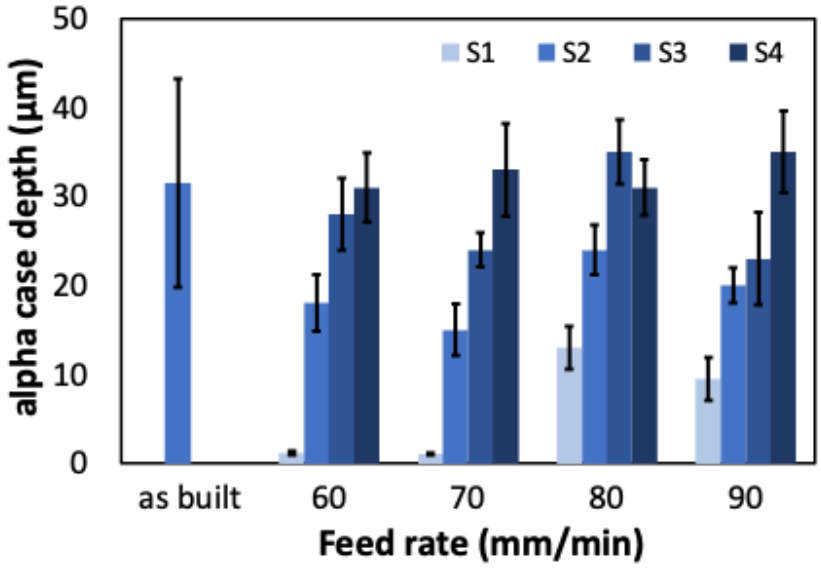

Figure 4.16 Alpha case depth shown for metal treated at various feed rates and the as built condition.

For feed rates of 60 and 70 mm/min, the S1 face had approximately 90% of the alpha case removed from the surface. The depth reported in Figure 4.16 reflects a small sample of "pockets" of alpha case remaining on the treated surface.

The micrographs used to measure the thickness of alpha case are shown in Figure 4.17. The removal of alpha case was most complete on the S1 face as evident from this montage. Improvements are also apparent in the S2 face via the substantial decrease in surface roughness. However, the S3 and S4 faces do not appear to show removal of alpha case or reduction in surface roughness.

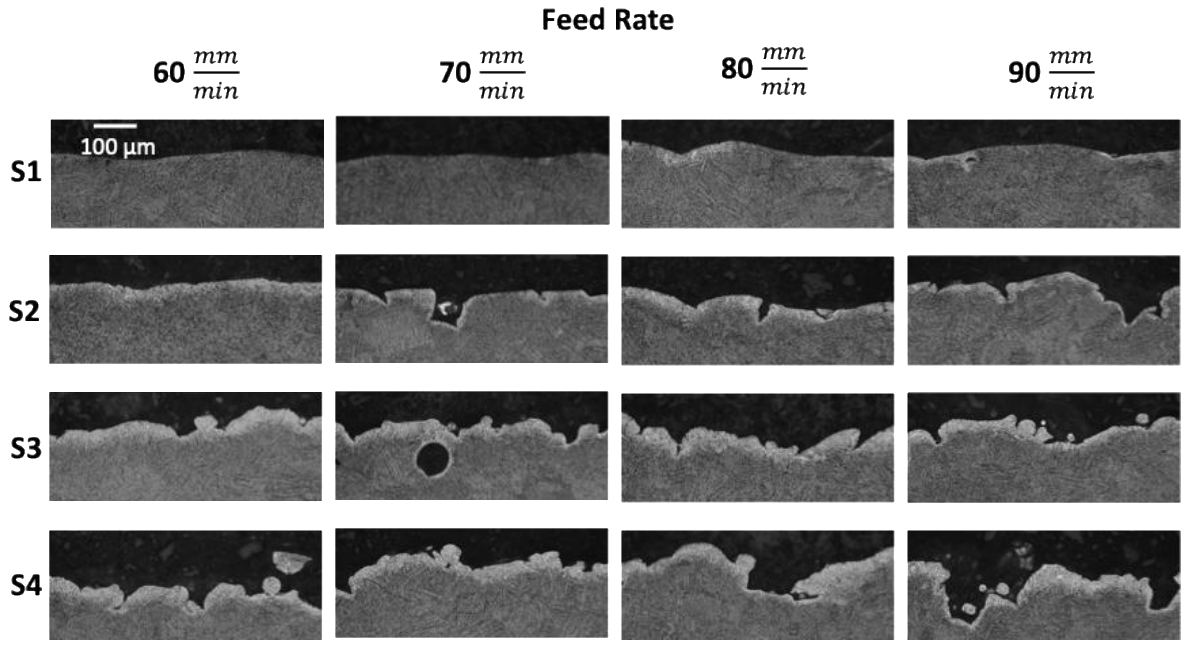

Figure 4.17 Micrographs of faces of hex bars treated with CASF at various feed rates. The surfaces were treated with Kroll's etchant and ABF tint etch to expose alpha case as a white layer on the surface.

Chapter 5. Discussion

5.1 Residual Stress

How does the residual stress resulting from CASF compare with that of other surface treatment processes. Notably, the compressive residual stress achieved by CASF surpasses that of tribofinishing (500 MPa) and falls within the range typically associated with shot peening (350–650 MPa) [12,14,51,52]. It also slightly exceeds the values recently reported for laser cavitation peening (400–450 MPa) [14, 53]. These results demonstrate that CASF is a highly effective post-processing method for LPBF titanium components, offering significant improvements in both surface roughness and compressive residual stress. Although the specific outcomes may vary depending on the material's constitutive behavior, similar benefits are to be expected for a wide range of metal parts produced by LPBF.

The compressive residual stress induced by CASF ranged from 200 to 720 MPa depending on treatment parameters and on the build orientation of the surface. The largest residual stresses resulted in treatment of the surfaces built with upskin orientation. It is reasonable to infer that the lower stress observed in the other two surface orientations was due to shielding effects from partially melted powder particles that covered the surfaces. If these particles are removed by a pre-treatment and the CASF treatment intensity is properly adjusted, it could be possible to achieve similar stress levels in LPBF targets regardless of the build orientation. Due to the importance of this topic, future work is recommended in this area.

A prominent complication encountered in measuring the residual stress in some of the samples was attributed to the surface roughness of the metal. Because the $\mathrm{Sin}^2(\psi)$ method utilizes x-ray diffraction for the measurement of lattice distortions, surface roughness reduces the intensity of the diffraction signal and expands the range in diffraction angles. Some of the samples had an

average surface roughness greater than R_a = 30μm. As a result, the residual stress measured on the roughest surfaces, including those in the as built condition and CASF treated samples with downskin orientation had lower signal to noise ratio in the X-ray detector. That resulted in higher variance in the residual stress measurements when compared to the smoother samples, including those with vertical and upskin orientations.

One issue that was observed throughout this research was the difference in residual stress measurements reported by the Sugino Corporation and those obtained at the University of Washington for the same samples. Both groups used the $\sin^2(\psi)$ method of evaluation using an X-ray diffractometer. However, the residual stress measurements obtained at the UW were consistently two to three times greater in magnitude than those reported by Sugino. The reason for this discrepancy was identified a result of the different X-ray sources used by the two groups. The wavelength of the X-ray source affects the penetration depth. Specifically, the mass absorption coefficient (μ / ρ) is described by

$$\frac{\mu}{\rho} = k\lambda^3 Z^3 \qquad 5.1.$$

Here, k is a material property, and Z is the atomic number of the absorber. Crucially, the linear absorption coefficient (μ) grows rapidly as the wavelength increases. This means that higher energy X-rays have a lower penetration depth and more of the received signal comes from x-rays closer to the surface. The X-Ray diffractometer used by Sugino utilizes a vanadium target, which creates electrons with an energy of 4.95 keV. The majority of the photons reached a depth of penetration within the titanium lattice of 26 μm or less. Meanwhile, the UW diffractometer uses a copper target, which generates X-rays with an energy of 8.01 keV. These higher energy electrons of the copper target result in a penetration depth of only about 11 μm. As presented in Figure 4.7, the measured residual stress decreased sharply within a distance of 30 μm from the surface. Hence,

due to the larger penetration depth of X-rays in Sugino's measurements and the averaging of content from the smaller lattice distortions at greater depth, the estimated residual stress is substantially lower.

Finally, the residual stress resulting from CASF should be put into context with other surface treatments that may be perceived as viable alternatives. Two commonly used surface treatments that could be considered contemporaries of CASF are chemical etching and shot peening. Because chemical etching is a treatment that only removes material, there is no capacity for introducing residual stress [14]. Shot peening on the other hand can result in residual stress of up to 800 MPa and extend up to 100 microns from the surface [14], which is much deeper than what was measured in the present research. However, as previously mentioned shot peening is limited to direct line of sight treatment. According to results of the hex bars in Figure 4.11, CASF is capable of introducing residual stress on non-direct line of sight surfaces as long as they are not fully obscured away from the cavitation cloud.

5.2 Residual Features

While evaluating the CASF treated surfaces of the metal, residual features were occasionally identified that were created during the printing process and persisted through CASF treatment. These residual features were primarily observed on the upskin and downskin metal and not as frequently on vertically printed metal. Due to their notch-like geometry, they could limit the effectiveness of using CASF as a surface treatment for the purpose of increasing fatigue life if CASF is unable to remove some of the largest features including the valleys as seen in Figure 4.1. However, evidence from Figure 4.16 shows that at slower feed rates, CASF is more capable of removing these features and producing a significantly smoother surface finish. It may be required

for future applications of CASF to change the operating parameters based on the type of target surface. One approach is to treat downskin surfaces at a feed rate of 60 millimeters per minute and then increasing to 120 millimeters per minute for upskin and vertically printed surfaces.

5.3 Alpha Case

Optical microscopy confirmed that approximately 90% of the alpha case was removed from the S1 surface when treated with feed rates of 60 and 70 mm/min. At these lower feed rates, the treatment intensity (i.e., the time spent per unit area) was sufficient to achieve significant material removal. However, at higher feed rates of 80 and 90 mm/min, the removal appeared limited to about 50% of the surface, likely due to reduced treatment intensity. Even at the slowest feed rates, small pockets of residual alpha case remained, indicating incomplete removal.

The difference in CASF effectiveness between the two surface conditions suggests that the oxide layer may inhibit effective treatment in certain regions, particularly in the deep valleys of the as-built L-PBF surface. These valleys likely shield parts of the surface from the cavitation cloud. Additionally, because the alpha case is harder than the surrounding material, it may require direct abrasive contact for effective removal, which is restricted in narrow or recessed features. Smaller abrasive particles might improve penetration into these deep valleys and aid in removing residual alpha case. Alternatively, further reduction in feed rate could increase treatment time and intensity, improving removal from these difficult-to-reach areas.

Chapter 6. Conclusions and Future Work

6.1 Conclusions

Supported by the Joint Center for Aerospace Technology Innovation (JCATI) program of Washington State, the primary motivation for this investigation was to advance the CASF process from a technology readiness level (TRL) of 3-4 to 6-7. In support of this effort, plate samples of Grade 5 titanium produced by LPBF were treated with CASF over a variety of feed rates and as a function of dwell time. To assess the CASF effectiveness, the treatment response was evaluated in terms of the change in microstructure, residual stress, and surface morphology with respect to the as-built condition.

Based on the findings, the following conclusions are drawn.

i. CASF reduced the surface roughness of the Ti6Al4V samples printed via LPBF. Metal printed vertically was reduced from an R_A of 5.0 – 5.6 μm to a range of 2.3 – 4.0 μm. Through the reduction in roughness, CASF reduces the severity of potential crack initiation points such as valleys with sharp radii of curvature, especially when it is performed at low feed rates.

ii. CASF treatment of the Ti6Al4V resulted in surface compressive residual stresses that ranged from approximately 200 MPa to approximately 600 MPa in the treatment of flat plates. The maximum residual stress recorded was 720 MPa and resulted from a dwell treatment at the center of the treatment patch.

iii. The compressive residual stress resulting from CASF was largest when treatment was applied to targets with upskin surface orientation, followed by the vertical and downskin printed orientations. The average residual stress for these three orientations was 524 ± 93, 355 ± 36 and 297 ± 83, respectively. There was no influence of feed rate on the magnitude of residual stress over the range of 60 to 120 mm/min. Hence, the residual stress does not appear to be a limiting factor in the rate of productivity achieved by CASF.

iv. The depth of compressive residual stress in the Ti6Al4V targets was measured to extend approximately 30 μm beneath the treated surface.

v. CASF was capable of removing alpha case from the surface of Ti6Al4V components. At feed rates of 70 mm/min and less there was limited or no remaining presence of the alpha case.

vi. CASF has the potential to serve as an all-encompassing surface finishing method for metal produced through LPBF by providing a treatment that can remove surface defects and introduce a compressive residual stress. The CASF treatment also had success on metal oriented at an angle and outside the direct line of treatment.

6.2 Recommendations for Future Work

Further research into CASF will need to reconsider variables in the processing conditions to further optimize surface smoothing of metal produced by powder bed fusion processes. The present observations suggest that further consideration should be given to the abrasive slurry concentration and the particle size distribution as these may contribute to both the material removal and residual stress impacts as well as alpha case removal. Further treatment parameter optimization may also be studied to increase the depth of residual stress imparted to further improve the performance of CASF treated metal.

The findings here are based on flat plates and accessible surfaces on the hex bars. However, LPBF often produces complex parts with internal channels and detailed features. Further study of CASF's effectiveness on internal surfaces and lattice structures will help to determine its suitability for real world AM components.

While CASF has been shown to reduce surface roughness and induce compressive residual stress, its direct effect on the fatigue life of components, particularly in comparison to other finishing methods (e.g., shot peening, laser shock peening), remains to be validated. As such, future work should conduct fatigue testing of CASF treated components across different orientations and surface conditions to quantify improvements in fatigue life.

Bibliography

[1] ASTM, “Specification for Powder Metallurgy (PM) Titanium and Titanium Alloy Structural Components.” ASTM International, West Conshohocken, PA, Nov. 01, 2018. doi: 10.1520/B0988-18.
Additive Manufacturing Technologies

[2] O. Diegel, A. Nordin, and D. Motte, “Additive Manufacturing Technologies,” *Springer Series in Advanced Manufacturing*, pp. 19–39, 2019, doi: 10.1007/978-981-13-8281-9_2.

[3] X. Zhao and T. Wang, “Laser Powder Bed Fusion of Powder Material: A Review,” *3D Printing and Additive Manufacturing*, vol. 10, no. 6, pp. 1439–1454, Dec. 2023, doi: 10.1089/3dp.2021.0297.

[4] F. Moura de Souza Soares, D. M. Barbosa, H. P. Reis Corado, A. I. de Carvalho Santana, and C. N. Elias, “Surface morphology, roughness, and corrosion resistance of dental implants produced by additive manufacturing,” *Journal of Materials Research and Technology*, vol. 21, pp. 3844–3855, Nov. 2022, doi: 10.1016/j.jmrt.2022.10.114.

[5] D. Obilanade, C. Dordlofva, and P. Törlind, “Surface roughness considerations in design for additive manufacturing - A literature review,” in *Proceedings of the Design Society*, 2021. doi: 10.1017/pds.2021.545.

[6] A. Triantaphyllou *et al.*, “Surface texture measurement for additive manufacturing,” *Surface Topography: Metrology and Properties*, vol. 3, no. 2, p. 024002, May 2015, doi: 10.1088/2051-672X/3/2/024002.

[7] J. C. Snyder and K. A. Thole, “Understanding Laser Powder Bed Fusion Surface Roughness,” *Journal of Manufacturing Science and Engineering*, vol. 142, no. 7, Jul. 2020, doi: 10.1115/1.4046504.

[8] C. Ye, C. Zhang, J. Zhao, and Y. Dong, “Effects of Post-processing on the Surface Finish, Porosity, Residual Stresses, and Fatigue Performance of Additive Manufactured Metals: A Review,” *Journal of Materials Engineering and Performance*, vol. 30, no. 9, pp. 6407–6425, Sep. 2021, doi: 10.1007/s11665-021-06021-7.

[9] B. M. Colosimo, Q. Huang, T. Dasgupta, and F. Tsung, “Opportunities and challenges of quality engineering for additive manufacturing,” *Journal of Quality Technology*, vol. 50, no. 3, pp. 233–252, Jul. 2018, doi: 10.1080/00224065.2018.1487726.

[10] M. Jurg, A. E. Medvedev, W. Yan, and A. Molotnikov, “Surface improvement of laser powder bed fusion processed Ti6Al4V for fatigue applications,” *Additive Manufacturing Letters*, vol. 3, p. 100070, Dec. 2022, doi: 10.1016/j.addlet.2022.100070.

[11] M. Kahlin *et al.*, “Improved fatigue strength of additively manufactured Ti6Al4V by surface post processing,” *International Journal of Fatigue*, vol. 134, p. 105497, May 2020, doi: 10.1016/j.ijfatigue.2020.105497.

[12] E. Maleki, S. Bagherifard, M. Bandini, and M. Guagliano, “Surface post-treatments for metal additive manufacturing: Progress, challenges, and opportunities,” *Additive Manufacturing*, vol. 37, p. 101619, Jan. 2021, doi: 10.1016/j.addma.2020.101619.

[13] H. Soyama and A. M. Korsunsky, “A critical comparative review of cavitation peening and other surface peening methods,” *Journal of Materials Processing Technology*, vol. 305, p. 117586, Jul. 2022, doi: 10.1016/j.jmatprotec.2022.117586.

[14] H. Soyama and D. Sanders, “Use of an Abrasive Water Cavitating Jet and Peening Process to Improve the Fatigue Strength of Titanium Alloy 6Al-4V Manufactured by the

Electron Beam Powder Bed Melting (EBPB) Additive Manufacturing Method," *JOM*, vol. 71, no. 12, pp. 4311–4318, Dec. 2019, doi: 10.1007/s11837-019-03673-8.
[15] E. O. Ezugwu and Z. M. Wang, "Titanium alloys and their machinability - A review," *Journal of Materials Processing Technology*, vol. 68, no. 3, 1997, doi: 10.1016/S0924-0136(96)00030-1.
[16] F. Yan, W. Xiong, and E. J. Faierson, "Grain structure control of additively manufactured metallic materials," *Materials*, vol. 10, no. 11, p. 1260, Nov. 2017, doi: 10.3390/ma10111260.
[17] J. Gockel, L. Sheridan, S. P. Narra, N. W. Klingbeil, and J. Beuth, "Trends in Solidification Grain Size and Morphology for Additive Manufacturing of Ti-6Al-4V," *JOM*, vol. 69, no. 12, pp. 2706–2710, Dec. 2017, doi: 10.1007/s11837-017-2601-6.
[18] H. Amano, Y. Yamaguchi, T. Ishimoto, and T. Nakano, "Reduction of spatter generation using atmospheric gas in laser powder bed fusion of Ti6Al4V," *Materials Transactions*, vol. 62, no. 8, pp. 1225–1230, 2021, doi: 10.2320/matertrans.MT-M2021059.
[19] M. BACHE, "Processing titanium alloys for optimum fatigue performance," *International Journal of Fatigue*, vol. 21, pp. 105–111, Sep. 1999, doi: 10.1016/S0142-1123(99)00061-4.
[20] J. Elambasseril, J. Rogers, C. Wallbrink, D. Munk, M. Leary, and M. Qian, "Laser powder bed fusion additive manufacturing (LPBF-AM): the influence of design features and LPBF variables on surface topography and effect on fatigue properties," *Critical Reviews in Solid State and Materials Sciences*, vol. 48, no. 1, pp. 132–168, Jan. 2023, doi: 10.1080/10408436.2022.2041396.
[21] M. Mojib, H. Soyama, D. Sanders, D. Arola, and M. Ramulu, "The High Cycle Fatigue Behavior of Surface Treated Electron Beam Melted Titanium Ti6Al4V," in *Volume 2A: Advanced Manufacturing*, American Society of Mechanical Engineers, Nov. 2021. doi: 10.1115/IMECE2021-71975.
[22] L. Lizzul, R. Bertolini, A. Ghiotti, and S. Bruschi, "Effect of AM-induced Anisotropy on the Surface Integrity of Laser Powder Bed Fused Ti6Al4V Machined Parts," *Procedia Manufacturing*, vol. 47, pp. 505–510, 2020, doi: 10.1016/j.promfg.2020.04.149.
[23] E. E. Covarrubias and M. Eshraghi, "Effect of Build Angle on Surface Properties of Nickel Superalloys Processed by Selective Laser Melting," *JOM*, vol. 70, no. 3, pp. 336–342, Mar. 2018, doi: 10.1007/s11837-017-2706-y.
[24] J. Metelkova, L. Vanmunster, H. Haitjema, and B. van Hooreweder, "Texture of inclined up-facing surfaces in laser powder bed fusion of metals," *Additive Manufacturing*, vol. 42, p. 101970, Jun. 2021, doi: 10.1016/j.addma.2021.101970.
[25] A. I. Dekhtyar, V. I. Bondarchuk, V. V. Nevdacha, and A. V. Kotko, "The effect of microstructure on porosity healing mechanism of powder near-β titanium alloys under hot isostatic pressing in α + β-region: Ti-10V-2Fe-3Al," *Materials Characterization*, vol. 165, p. 110393, Jul. 2020, doi: 10.1016/j.matchar.2020.110393.
[26] H. v. Atkinson and S. Davies, "Fundamental aspects of hot isostatic pressing: An overview," *Metallurgical and Materials Transactions A*, vol. 31, no. 12, pp. 2981–3000, Dec. 2000, doi: 10.1007/s11661-000-0078-2.
[27] A. Abu-Issa *et al.*, "Effects of altered hot isostatic pressing treatments on the microstructures and mechanical performance of electron beam melted Ti-6Al-4V," *Journal of Materials Research and Technology*, vol. 9, no. 4, pp. 8735–8743, Jul. 2020, doi: 10.1016/j.jmrt.2020.06.019.

[28] R. Gaddam, B. Sefer, R. Pederson, and M.-L. Antti, “Study of alpha-case depth in Ti-6Al-2Sn-4Zr-2Mo and Ti-6Al-4V,” *IOP Conference Series: Materials Science and Engineering*, vol. 48, p. 012002, Dec. 2013, doi: 10.1088/1757-899X/48/1/012002.
[29] E. V. Naydenkin, I. P. Mishin, I. V. Ratochka, O. N. Lykova, and O. V. Zabudchenko, “The effect of alpha-case formation on plastic deformation and fracture of near β titanium alloy,” *Materials Science and Engineering: A*, vol. 769, p. 138495, Jan. 2020, doi: 10.1016/j.msea.2019.138495.
[30] J. C. Fox, S. P. Moylan, and B. M. Lane, “Effect of Process Parameters on the Surface Roughness of Overhanging Structures in Laser Powder Bed Fusion Additive Manufacturing,” *Procedia CIRP*, vol. 45, pp. 131–134, 2016, doi: 10.1016/j.procir.2016.02.347.
[31] F. Cabanettes *et al.*, “Topography of as built surfaces generated in metal additive manufacturing: A multi scale analysis from form to roughness,” *Precision Engineering*, vol. 52, pp. 249–265, Apr. 2018, doi: 10.1016/j.precisioneng.2018.01.002.
[32] S. Rott, A. Ladewig, K. Friedberger, J. Casper, M. Full, and J. H. Schleifenbaum, “Surface roughness in laser powder bed fusion – Interdependency of surface orientation and laser incidence,” *Additive Manufacturing*, vol. 36, p. 101437, Dec. 2020, doi: 10.1016/j.addma.2020.101437.
[33] F. Calignano, “Investigation of the accuracy and roughness in the laser powder bed fusion process,” *Virtual and Physical Prototyping*, vol. 13, no. 2, pp. 97–104, Apr. 2018, doi: 10.1080/17452759.2018.1426368.
[34] A. N. Soe, A. Sombatmai, P. Promoppatum, V. Srimaneepong, V. Trachoo, and P. Pandee, “Effect of post-processing treatments on surface roughness and mechanical properties of laser powder bed fusion of Ti–6Al–4V,” *Journal of Materials Research and Technology*, vol. 32, pp. 3788–3803, Sep. 2024, doi: 10.1016/j.jmrt.2024.08.197.
[35] V. Deshmukh, R. Kadam, and S. S. Joshi, “Removal of alpha case on titanium alloy surfaces using chemical milling,” *Machining Science and Technology*, vol. 21, no. 2, pp. 257–278, Apr. 2017, doi: 10.1080/10910344.2017.1284558.
[36] J. C. Bertolini, “Hydrofluoric acid: A review of toxicity,” *The Journal of Emergency Medicine*, vol. 10, no. 2, pp. 163–168, Mar. 1992, doi: 10.1016/0736-4679(92)90211-B.
[37] Horace J. Grover, “FACTORS BY WHICH SHOT PEENING INFLUENCES THE FATIGUE STRENGTH OF PARTS,” Sep. 1954.
[38] A. Azhari, C. Schindler, K. Hilbert, C. Godard, and E. Kerscher, “Influence of waterjet peening and smoothing on the material surface and properties of stainless steel 304,” *Surface and Coatings Technology*, vol. 258, pp. 1176–1182, Nov. 2014, doi: 10.1016/j.surfcoat.2014.07.013.
[39] M. Ramulu, S. Kunaporn, D. Arola, M. Hashish, and J. Hopkins, “Waterjet Machining and Peening of Metals,” *Journal of Pressure Vessel Technology*, vol. 122, no. 1, pp. 90–95, Feb. 2000, doi: 10.1115/1.556155.
[40] D. D. Arola and M. L. McCain, “Abrasive waterjet peening: A new method of surface preparation for metal orthopedic implants,” *Journal of Biomedical Materials Research*, vol. 53, no. 5, pp. 536–546, Sep. 2000, doi: 10.1002/1097-4636(200009)53:5<536::AID-JBM13>3.0.CO;2-V.
[41] D. Arola, A. E. Alade, and W. Weber, “IMPROVING FATIGUE STRENGTH OF METALS USING ABRASIVE WATERJET PEENING,” *Machining Science and Technology*, vol. 10, no. 2, pp. 197–218, Jul. 2006, doi: 10.1080/10910340600710105.

[42] H. Soyama, “Cavitation Peening: A Review,” *Metals*, vol. 10, no. 2, p. 270, Feb. 2020, doi: 10.3390/met10020270.
[43] M. Sato, O. Takakuwa, M. Nakai, M. Niinomi, F. Takeo, and H. Soyama, “Using Cavitation Peening to Improve the Fatigue Life of Titanium Alloy Ti-6Al-4V Manufactured by Electron Beam Melting,” *Materials Sciences and Applications*, vol. 07, no. 04, 2016, doi: 10.4236/msa.2016.74018.
[44] H. Soyama and C. Kuji, “Improving effects of cavitation peening, using a pulsed laser or a cavitating jet, and shot peening on the fatigue properties of additively manufactured titanium alloy Ti6Al4V,” *Surface and Coatings Technology*, vol. 451, 2022, doi: 10.1016/j.surfcoat.2022.129047.
[45] “Specification for Additive Manufacturing Titanium-6 Aluminum-4 Vanadium with Powder Bed Fusion.” ASTM International, West Conshohocken, PA, Oct. 01, 2021. doi: 10.1520/F2924-14R21.
[46] “Standard Terminology for Additive Manufacturing—Coordinate Systems and Test Methodologies”, [Online]. Available: https://www.iso.org/obp
[47] S.-D. Tsai, D. Mahulikar, H. L. Marcus, I. C. Noyan, and J. B. Cohen, “Residual stress measurements on Al-graphite composites using X-ray diffraction,” *Materials Science and Engineering*, vol. 47, no. 2, pp. 145–149, Feb. 1981, doi: 10.1016/0025-5416(81)90220-2.
[48] B. B. He, *Two-dimensional X-ray Diffraction*. Wiley, 2018. doi: 10.1002/9781119356080.
[49] “Designation: E407-07 Standard Practice for Microetching Metals and Alloys 1,” *ASTM International*, 2011, doi: 10.1520/E0407-07.
[50] ISO 4288:1998; “Geometrical Product Specifications (GPS)—Surface Texture: Profile Method—Rules and Procedures for the Assessment of Surface Texture.” International Organization for Standardization: Geneva, Switzerland, 1998; Volume 1998.
[51] H. Soyama and F. Takeo, “Effect of Various Peening Methods on the Fatigue Properties of Titanium Alloy Ti6Al4V Manufactured by Direct Metal Laser Sintering and Electron Beam Melting,” *Materials*, vol. 13, no. 10, p. 2216, May 2020, doi: 10.3390/ma13102216.
[52] N. Wang, J. Zhu, B. Liu, X. Zhang, J. Zhang, and S. Tu, “Influence of Ultrasonic Surface Rolling Process and Shot Peening on Fretting Fatigue Performance of Ti-6Al-4V,” *Chinese Journal of Mechanical Engineering*, vol. 34, no. 1, pp. 90–103, Dec. 2021, doi: 10.1186/s10033-021-00611-1.
[53] A. M. Mancisidor *et al.*, “Effect of Post-Processing Treatment on Fatigue Performance of Ti6Al4V Alloy Manufactured by Laser Powder Bed Fusion,” *Journal of Manufacturing and Materials Processing*, vol. 7, no. 4, p. 119, Jun. 2023, doi: 10.3390/jmmp7040119.

Appendix – Figures and Data

Tabulated data:

LPBF 2 millimeter thick plate

Sample	feed rate (mm/min)	Residual Stress (MPa)
untreated	0	25.55
B1W-1	60	80.8
B1W-2	65	312.2
B1W-3	70	472.1
B1W-4	75	527.4
B1W-5	80	661.4
B1W-6	90	618.65
B1W-7	100	678.15
B1W-8	120	640.15

Wrought 2 millimeter thick plate

Sample	feed rate (mm/min)	Residual Stress (MPa)
untreated	0	48.05
B1W-1	60	180.3
B1W-2	65	275.4
B1W-3	70	383.75
B1W-4	75	517.95
B1W-5	80	661.4
B1W-6	90	584.25
B1W-7	100	607.65
B1W-8	120	613.3

LPBF 6 millimeter thick plate

Sample	feed rate (mm/min)	Residual Stress (MPa)
B1W-73	60	114
B1W-74	65	100
B1W-75	70	143
B1W-76	75	111
B1W-77	80	104
B1W-78	90	119
B1W-79	100	133

B1W-80	120	91

Wrought 6 millimeter thick plate

Sample	feed rate (mm/min)	Residual Stress (MPa)
B1W-73	60	179
B1W-74	65	184
B1W-75	70	331
B1W-76	75	340
B1W-77	80	254
B1W-78	90	199
B1W-79	100	280
B1W-80	120	272

Hex bar with Alpha case sample 1

Face	feed rate (mm/min)	Residual Stress (MPa)
S1	60	477.1
S2	60	59.6
S3	60	13.55
S4	60	5.1
S2'	60	143.1
S3'	60	6.55

Hex bar with Alpha case sample 2

Face	feed rate (mm/min)	Residual Stress (MPa)
S1	70	551
S2	70	131.95

Hex bar with Alpha case sample 3

Face	feed rate (mm/min)	Residual Stress (MPa)
S1	80	695.4
S2	80	128.95

Hex bar with Alpha case sample 4

Face	feed rate (mm/min)	Residual Stress (MPa)
S1	90	425.2
S2	90	162.95

Hex bar without Alpha case sample 1

Face	feed rate (mm/min)	Residual Stress (MPa)
S1	60	640.15
S2	60	180.25
S3	60	-8.5
S4	60	-21.5
S2'	60	80.35
S3'	60	9.6

Hex bar without Alpha case sample 2

Face	feed rate (mm/min)	Residual Stress (MPa)
S1	70	573.5
S2	70	101.85

Hex bar without Alpha case sample 3

Face	feed rate (mm/min)	Residual Stress (MPa)
S1	80	653.3
S2	80	93.15

Hex bar without Alpha case sample 4

Face	feed rate (mm/min)	Residual Stress (MPa)
S1	90	581.35
S2	90	53.3

Angled Treatment 45˚

Sample	feed rate (mm/min)	Residual Stress (MPa)
609	60	253.2
611	70	202.95
613	80	210.9
614	90	190.15
615	100	225.3
616	120	186.95

Angled Print 45˚ down skin

Sample	feed rate (mm/min)	Residual Stress (MPa)
B2D-60	60	386.75
B2D-61	80	581
B2D-62	100	549.2
B2D-63	120	580.7

Angled Print 45˚ down skin

Sample	feed rate (mm/min)	Residual Stress (MPa)
B2U-60	60	300.35
B2U-61	80	258.25
B2U-62	100	410.95
B2U-63	120	218.25

Spot Treatment 6 minutes vertical

Sample	Distance from center (mm)	Residual Stress (MPa)
508	0	718.5
508	3	668.25
508	6	627.75
508	9	480.3
508	12	141.6
508	15	89.35

Spot Treatment 6 minutes up skin

Sample	Distance from center (mm)	Residual Stress (MPa)
57	0	848
57	3	635.5
57	6	676
57	9	382.7
57	12	247.25

Spot Treatment 6 minutes down skin

Sample	Distance from center (mm)	Residual Stress (MPa)
57	0	653.15
57	3	552.3
57	6	390.7
57	9	103.85
57	12	68.95

Spot Treatment 6 minutes down skin

Sample	Treatment time between measurements (mm:ss)	total depth (μm)	Residual Stress (MPa)
1	0	0	261.4
1	:30	4.25	277.25
1	1:15	7.25	140.1
1	1:00	12	159
1	4:00	15	125.1
1	3:00	19.75	96.2

Spot Treatment 6 minutes down skin

Sample	Treatment time between measurements (mm:ss)	total depth (μm)	Residual Stress (MPa)
2	0	0	332.45
2	:30	4.25	340.25
2	1:15	7.25	240.15
2	1:00	12	247.25
2	4:00	15	119.9
2	3:00	19.75	122.55

Spot Treatment 6 minutes down skin

Sample	Treatment time between measurements (mm:ss)	total depth (μm)	Residual Stress (MPa)

3	0	0	384.2
3	1:30	2.75	321.3
3	1:15	8.25	199.8
3	3:30	13.25	145.4
3	3:30	17.75	118.2
3	6:00	21.25	86.8
3	3:00	24.25	52.55
3	6:00	27.5	78.8
3	3:30	32.75	67.45

Spot Treatment 6 minutes down skin

Sample	Treatment time between measurements (mm:ss)	total depth (µm)	Residual Stress (MPa)
4	0	0	344.35
4	1:30	2.75	263.5
4	1:15	8.25	151.45
4	3:30	13.25	94.4
4	3:30	17.75	100.25
4	6:00	21.25	88.3
4	3:00	24.25	67.7
4	6:00	27.5	65.95
4	3:30	32.75	76.85

Micrographs:

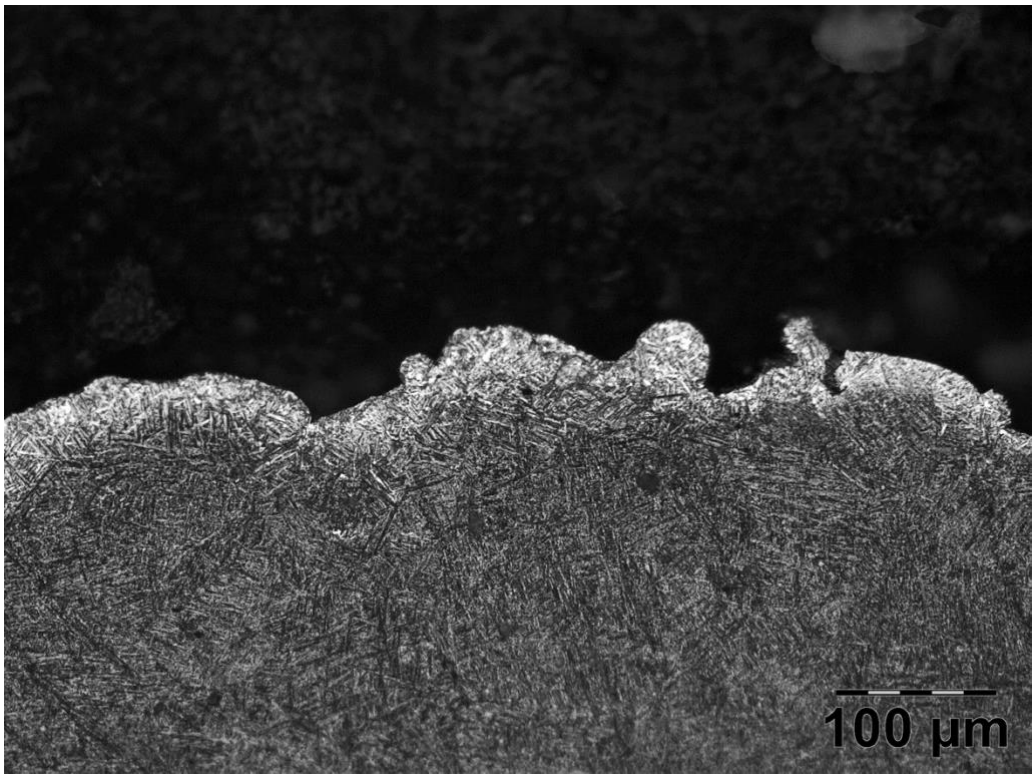

Untreated Hex bar

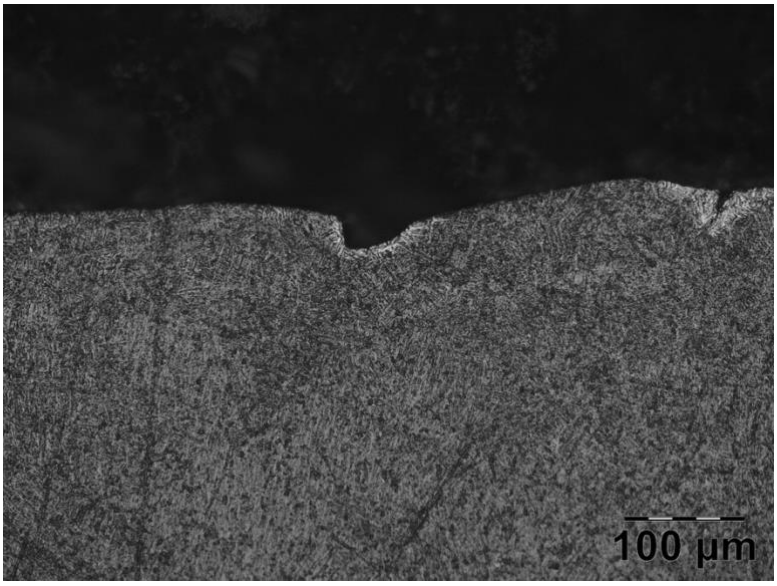

S1 surface of Hex bar with alpha case 1

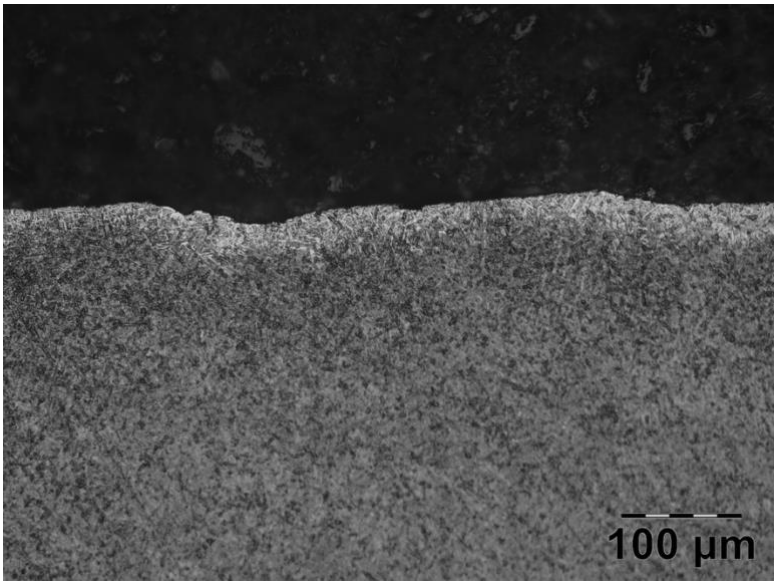

S2 surface of Hex bar with alpha case 1

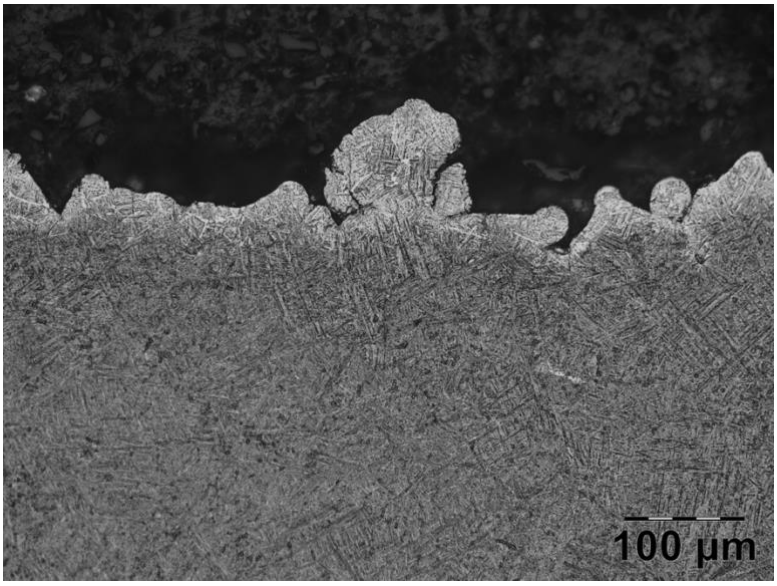

S3 surface of Hex bar with alpha case 1

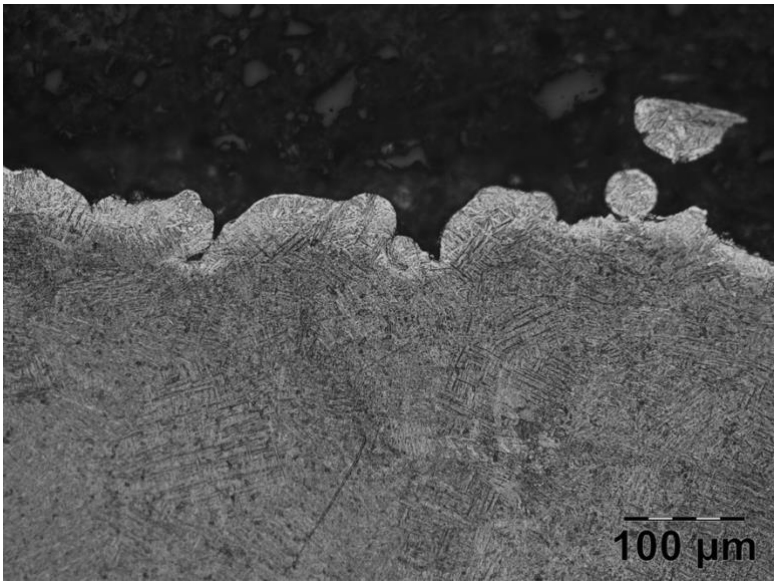

S4 surface of Hex bar with alpha case 1

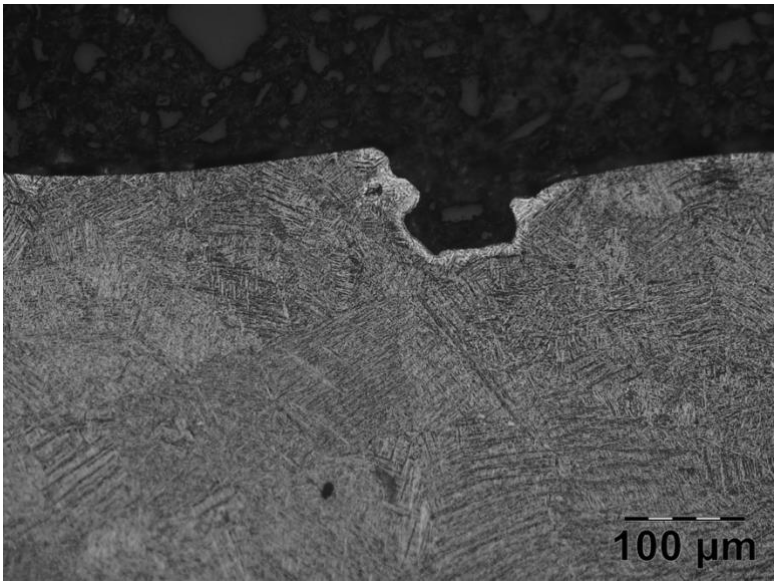

S1 surface of Hex bar with alpha case 2

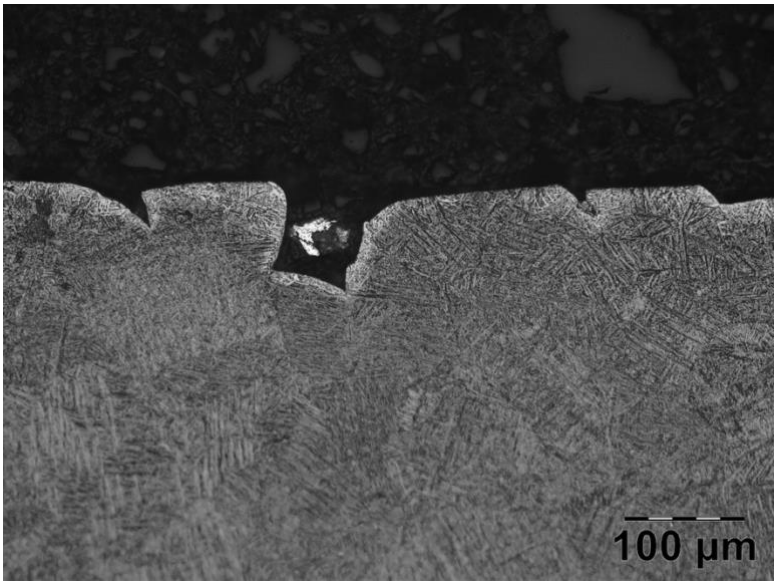

S2 surface of Hex bar with alpha case 2

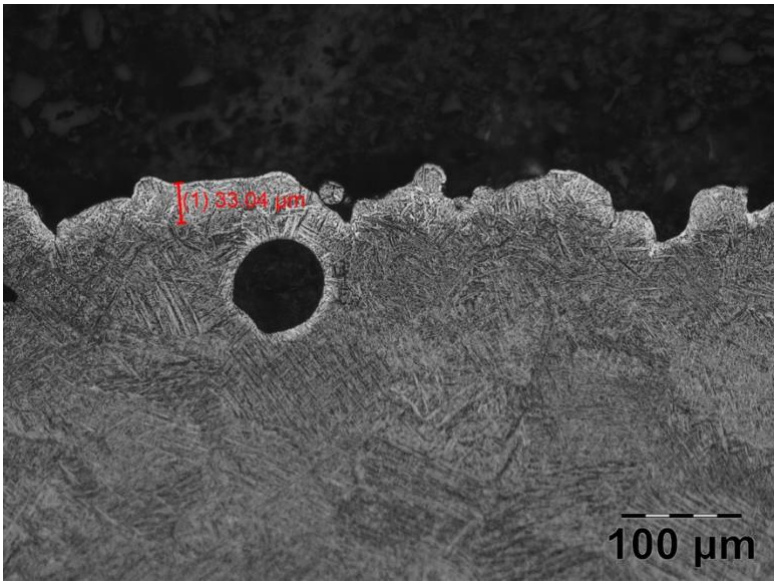

S3 surface of Hex bar with alpha case 2

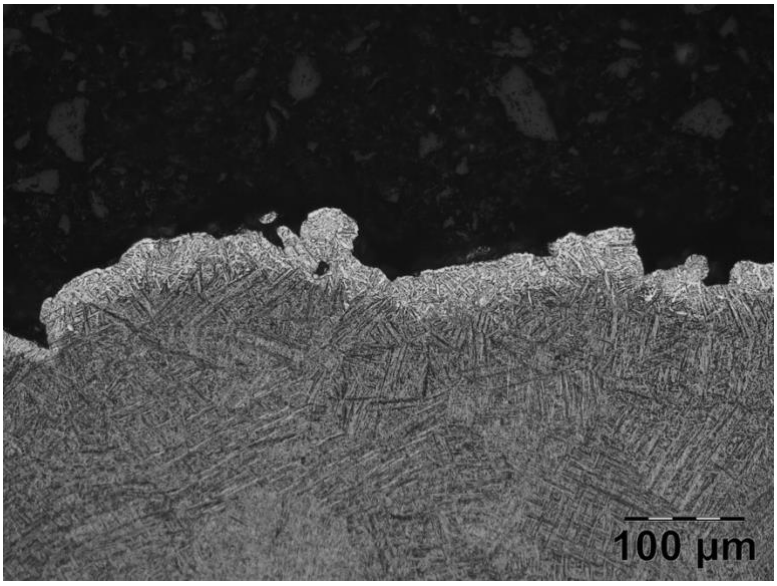

S4 surface of Hex bar with alpha case 2

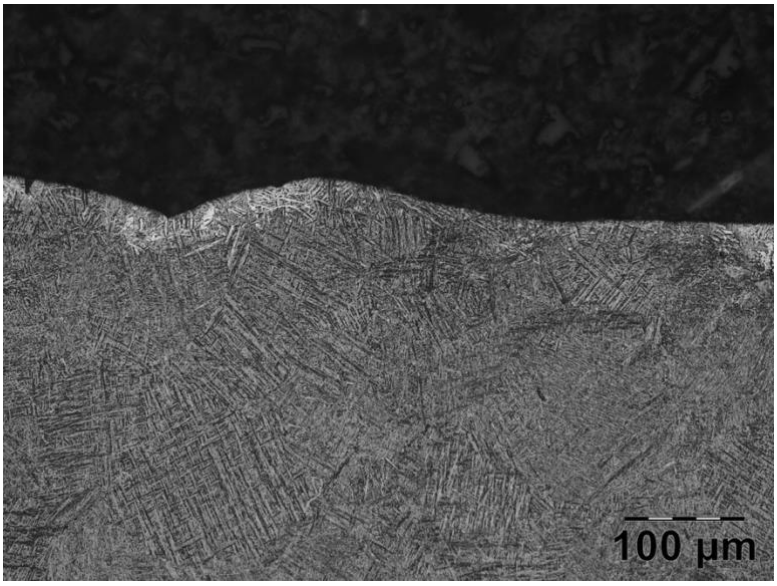

S1 surface of Hex bar with alpha case 3

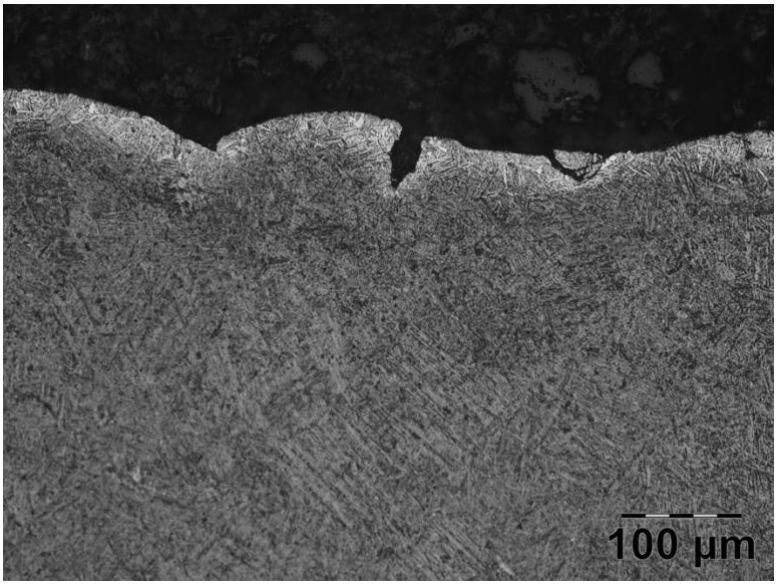

S2 surface of Hex bar with alpha case 3

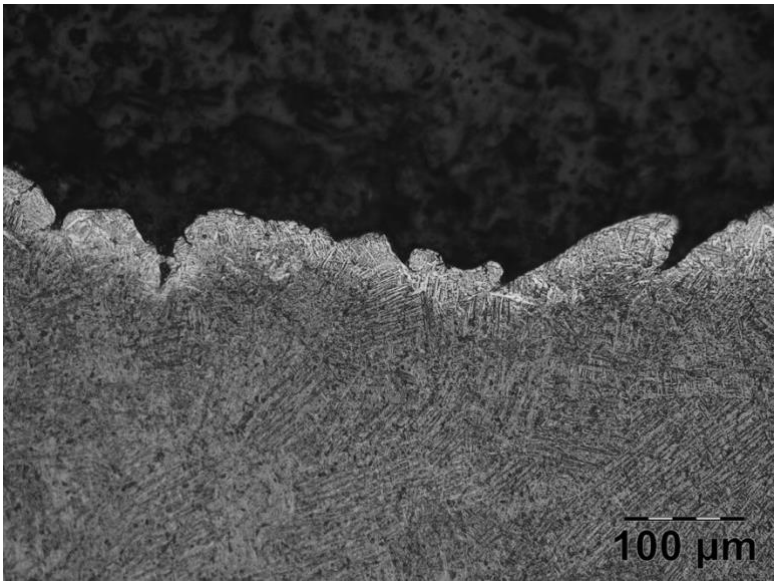

S3 surface of Hex bar with alpha case 3

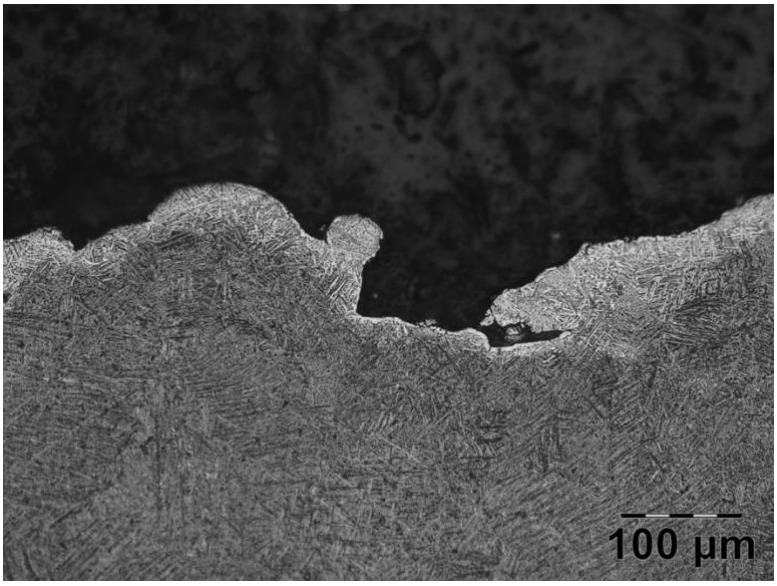

S4 surface of Hex bar with alpha case 3

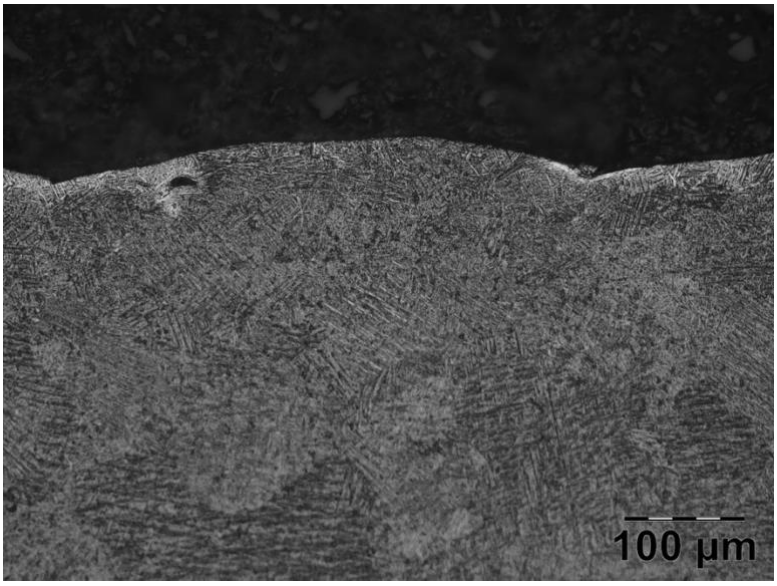

S1 surface of Hex bar with alpha case 4

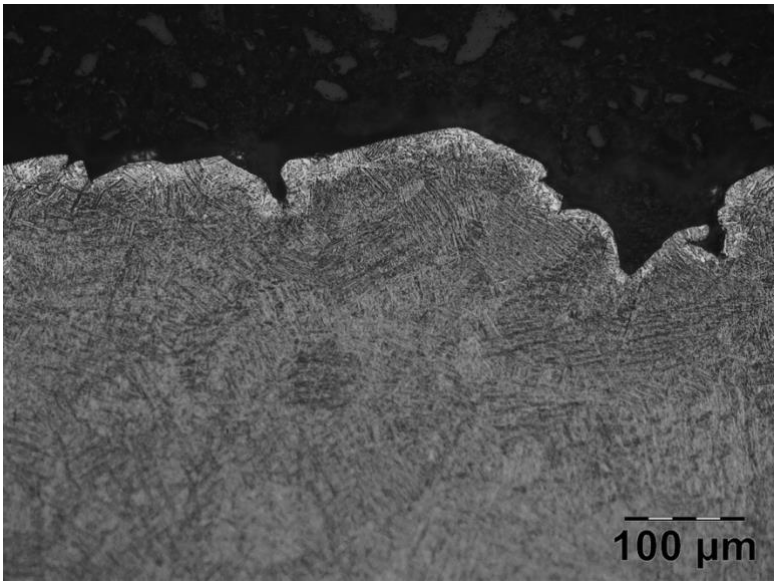

S2 surface of Hex bar with alpha case 4

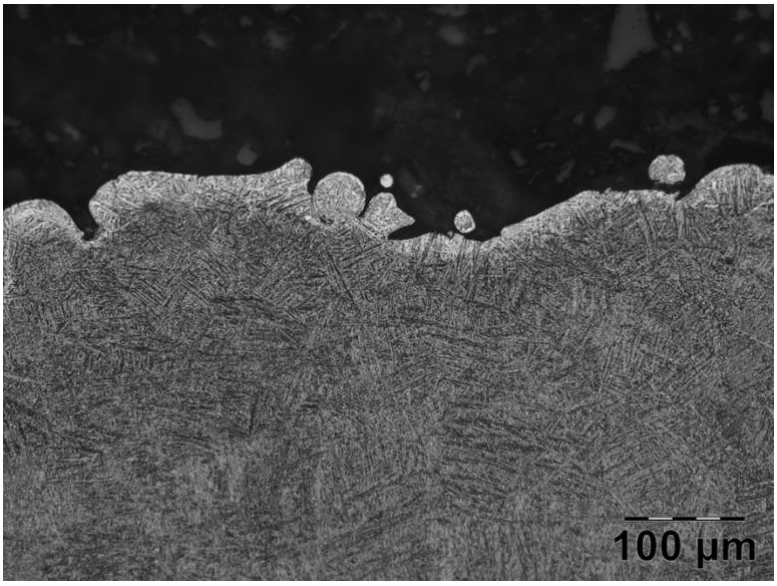

S3 surface of Hex bar with alpha case 4

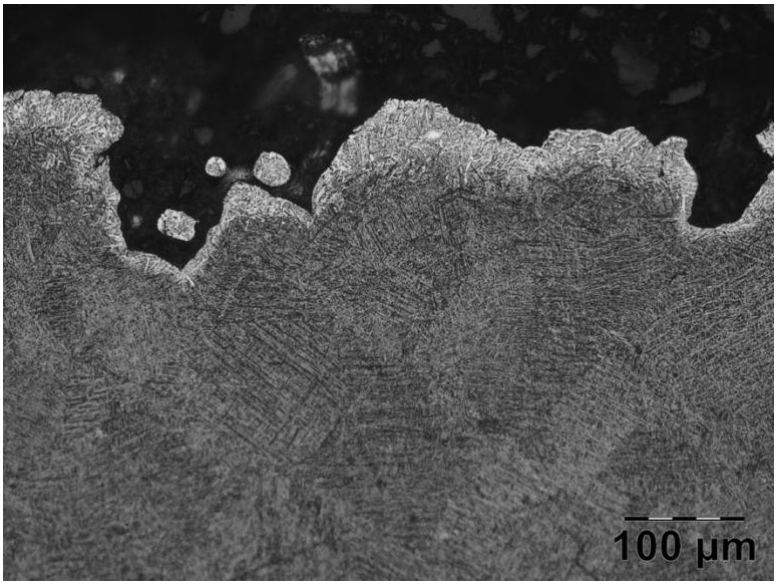

S4 surface of Hex bar with alpha case 4

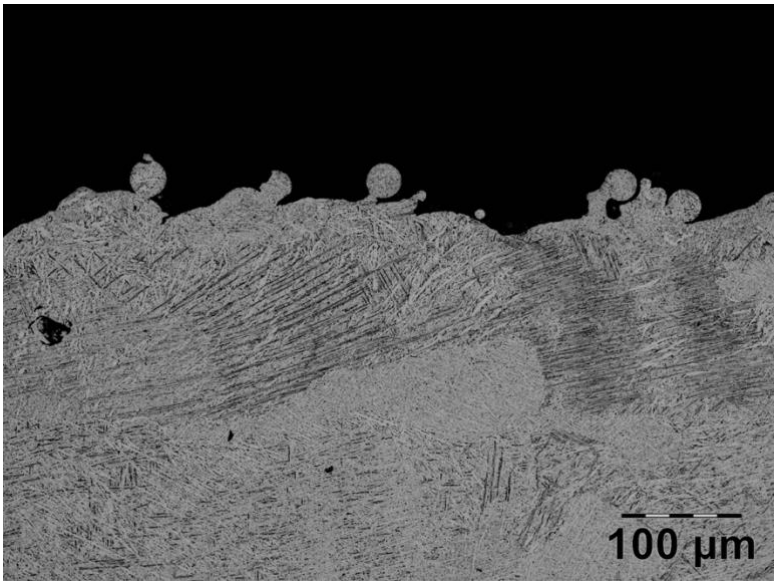

Vertically printed surface without treatment

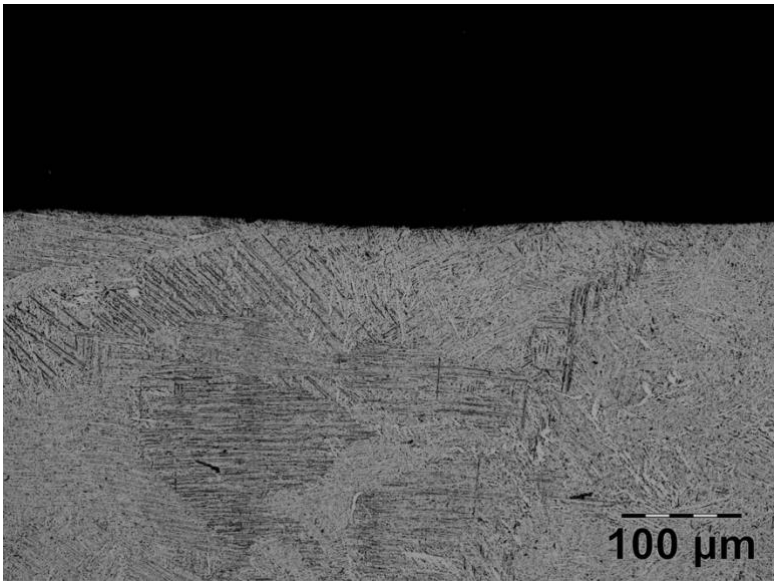

Vertically printed surface after treatment

SEM Images:

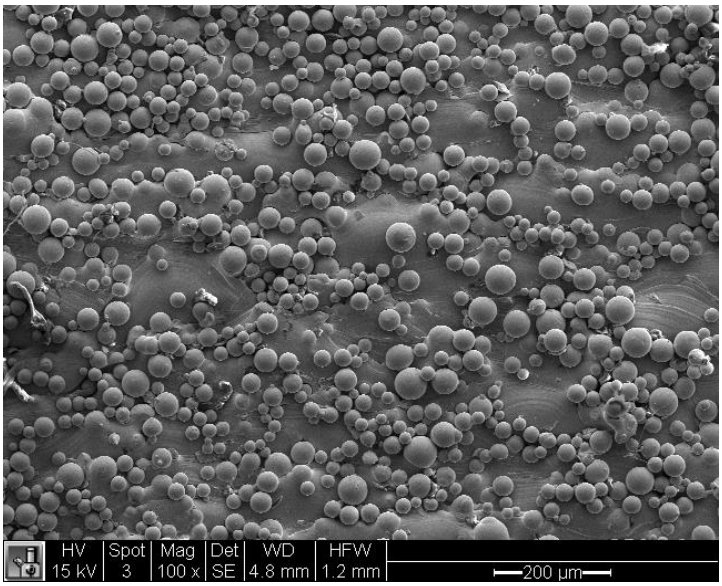

Vertically printed surface without treatment

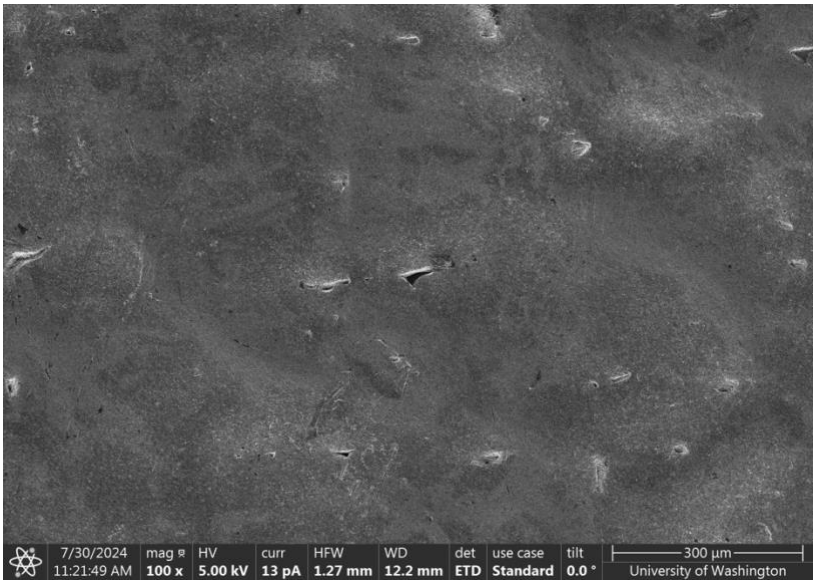

Vertically printed surface after treatment at 80 mm/min

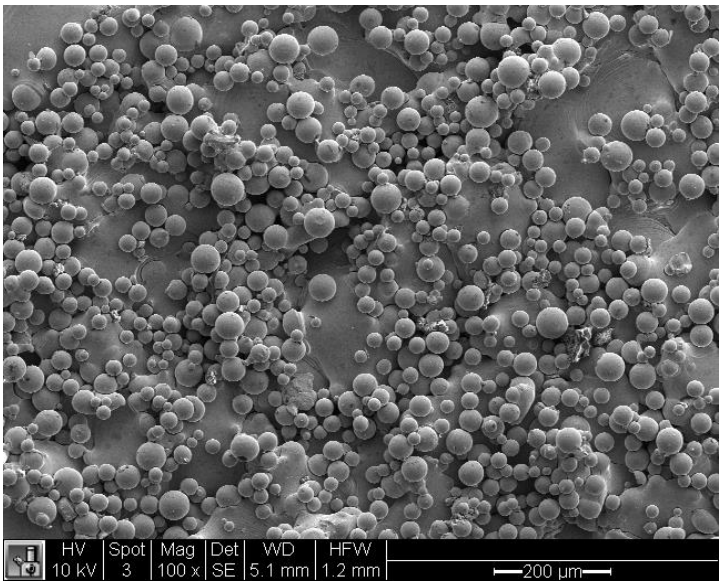

Down skin printed surface without treatment

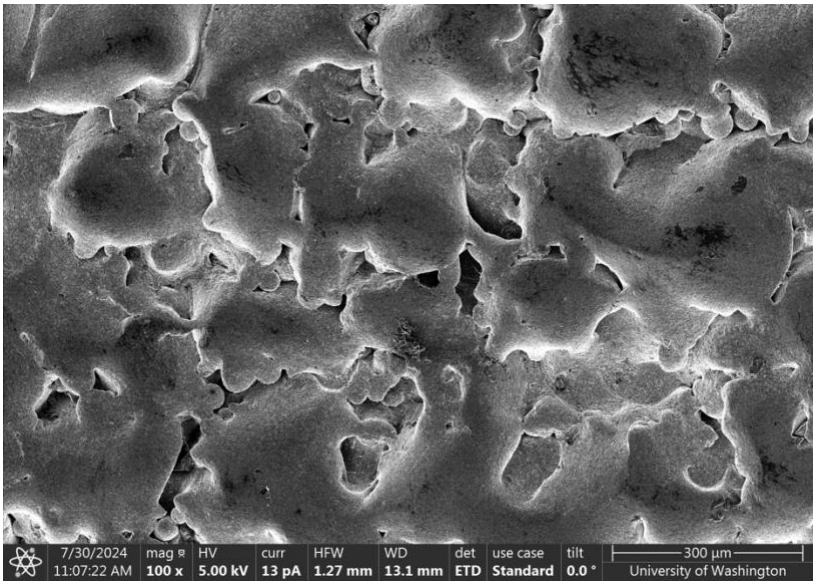

Down skin printed surface treated at 80 mm / min

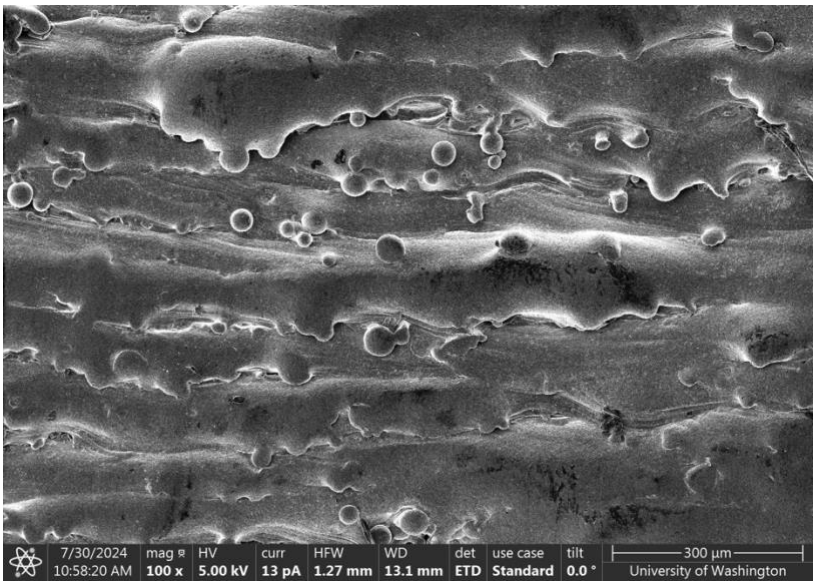

Up skin printed surface without treatment

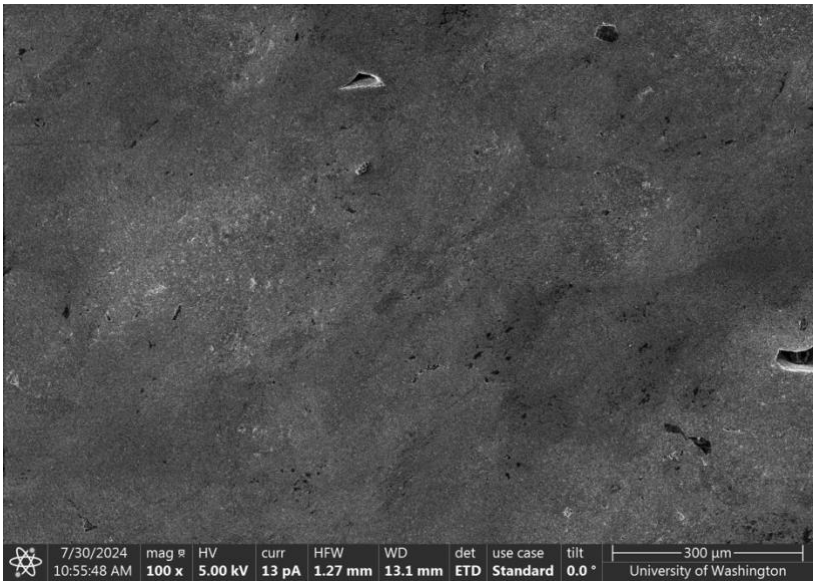

Up skin printed surface treated at 80 mm / min